Contents

Chapter 1

The Higgs Bosons and the MSSM

This chapter is devoted to introduce the theoretical background to the experimental search presented in this thesis. A brief overview of the Standard Model of particle physisics is given in Section 1.1 based on Reference [1]. Among all the extesion of the Standard Model, the Minimal Supersymmetric extension of the Standard Model (MSSM) is a theoretically favoured scenario as one of the most predictive framework beyond the Standard Model, it is introduced in Section 1.2 with focus on its Higgs sector and is based on References [2,3]. Finally, a review of the MSSM Higgs bosons phenomenological aspects, which are relevant to the presented search, is given in Section 1.3 based on Reference [4].

1.1   The Standard Model of Particle Physics

1.1.1   Introduction

A detailed description of the Standard Model of particle physics may be found in
Ref. [6], only a brief overview is given in what follows.

The Standard Model (SM) of particle physics is a theory aimed to describe and
quantitatively predict the phenomenology of fundamental interactions. At "microscopic" level the spectrum of all interactions between matter and radiation can
be understood in terms of three classes of foundamental forces: the strong, the
electromagnetic and the weak forces. These interactions are described by a local
relativistic quantum field theory, where to each particle is associated a field with
suitable transformation properties under the Lorentz group. The theory is based on
the principle of gauge invariance, which means invariance under a symmetry transformations that operates on basic internal degrees of freedom and depends on the
space-time coordinate. The gravitational force is negligible in atomic and nuclear
physics, in fact, quantum effects of gravity are expected at energies corresponding
to the Planck mass $E \sim M_{planck}c^2 \sim 10^{19}$ GeV.

The SM is a gauge field theory based on the symmetry group $SU(3)_c \otimes SU(2)_L \otimes
U(1)_Y$. The group has $8 + 3 + 1 = 12$ generators with a non trivial commutator
algebra. The electromagnetic and weak interactions [7–9] are described by the
$SU(2)_L \otimes U(1)_Y$ symmetry group, while the $SU(3)_c$ is the colour group of the
theory of strong interactions (QCD) [10]. To each generator of the symmetry group
is associated a vector boson which act as mediator of the correspondig interactions.
Eight gluons are associated to the $SU(3)_c$ colour generators, while for four gauge
bosons $W^{\pm}$, Z^0 and γ are associated to the generators of $SU(2)_L \otimes U(1)_Y$. Only the
gluons and the photon are massless since the symmetry induced by the other three
generators is spontaneusly broken. In the SM the spontaneus symmetry breaking
is realized by the Higgs mechanism [11–15]. The Higgs boson acts as mediator
of a new class of interactions that, at tree level, are coupled in proportion to the
particle masses. An Higgs boson, with properties that resemble the one of the SM,
has recently been discovered at the LHC with $m_H \sim 126$ GeV [16,17] and represents
one of the major mailstone of particle physics.

The fermionic matter fields of the SM are quarks and leptons. Quarks are
subject to all SM interactions, each type of quark is a colour triplet and carries
electroweak charges, in particular electric charges $+2/3$ for up-type quarks and
$-1/3$ for down-type quarks. Leptons are colourless but have electroweak charges,
in particular electric charges -1 for charged leptons e, μ and τ (opposite sign charge
is intended for respective anti-particle) and charge 0 for neutrinos ν_e, ν_{μ} and ν_{τ}.
Qarks and leptons are grouped in three "generations" with equal quantum numbers
but different masses.

1.1.2   Precision Test and Limitation of the SM

The Standard Model has been succesfully tested in a vast number of experiments
over a wide range of energies during the last few decades. Precision tests of the
electroweak theory performed at LEP, SLC and the Tevatron [20], has confirmed

that the couplings of quark and leptons to the weak gauge bosons $W^{\pm}$ and Z are indeed precisely those prescribed by the gauge symmetry. The accuracy of a few per-mille for these tests implies that, not only the tree level, but also the structure of quantum corrections has been verified. Several other experimental results [19] including rare decays of hadrons provides a test for low-energies of the standard model. The recent discovery of a Higgs boson is also another success of the SM, its mass, spin and couplings are in agreement with expected values from a global fit of electroweak costraints [21]. Among all the parameters of the Standard Model only few of them presents tension with experimental data, the most significant discrepancies are sligthly above three standard deviations and are given by: the anomalus magnetic moment of the muon [22], a_{μ} and the forward-backward asymmetry of top quarks [23], $A_{FB}^{t\bar{t}}$.

In spite of this success, the Standard Model is conceptually unsatisfactory for quite few deficiencies and is widely belived to be an effective theory valid only at the present accessible energies. Beside the fact that it does not include gravitational force, it does not explain the pattern of fermion masses and in its simplest version does not include neutrino masses, it has at least other three conceptual problems which indicates the need for physics Beyond the Standard Model (BSM):

Hierarchy Problem Calculating the radiative correction to the Higgs boson mass, quadratic divergencies of the order of the cut-off scale Λ occur, where Λ defines the energy beyond which the theory ceases to be valid and new physics should appear [24]. If the cut-off is choosen to be $\sim M_{Planck}$, then a fine tunig with an unnaturally high precision , $\mathcal{O}(10^{-30})$, should occur to cancell these divergencies leaving the Higgs boson with a mass of the order of the electroweak breaking scale, M_{EW}. A question that has no satisfactory answer in the SM is how these cancellations can occur and why $\Lambda >> M_{EW}$, these problems are called the fine-tuning and hierarchy problem [25–27].

Dark Matter The SM does not have a candidate which can explain the large contribution of non-barionic, non-luminous matter to the density of the Universe [28–30]. To be a Dark Matter candidate a particle should be stable, massive and should interact only via very weak interactions.

Unification Problem Another unsatisfactory aspect of the SM is that does not provide the unification of the electroweak and strong interactions, their couplings do not meet at high energies. Considering the successfull unification of electromagnetic and weak interaction, the existence of Grand Unified Theory (GUT) has been suggested [31, 32], which predicts the unification of all the three gauge coupling strenght at the GUT energy scale, $\Lambda_{GUT} \simeq 10^{16}$ GeV and describes the three forces within a single gauge group with just one coupling constant.

Among all the extension of the SM, Supersymmetry is a theoretically favoured scenario as the most predictive framework beyond the Standard Model. As discussed in Section 1.2, it gives a natural answer to the hierarchy problem, provides a suitable candidate for Dark Matter and predicts unification of the three gauge couplings at GUT energy scale.

1.2 The Minimal Supersymmetric Standard Model

1.2.1 Introduction to the MSSM

Supersymmetry (SUSY) [33–35] was first introduced as a natural way to solve the hierarchy problem. The SUSY generators $\mathcal{Q}$ transforms fermion into bosons and vice versa:

$$\mathcal{Q}|\text{Fermion}\rangle = |\text{Boson}\rangle, \quad \mathcal{Q}|\text{Boson}\rangle = |\text{Fermion}\rangle \tag{1.1}$$

In a supersymmetric extesion of the SM each of the known foundamental particles is in either a chiral or gauge *supermultiplet* and must have a superpartner with spin differing by 1/2 unit. SUSY naturally solve the hierarchy problem since the quadratic divergent loop contribution to the Higgs mass of the SM particles are canceled by the loop contribution of the corresponding partners. The name of the superpartner of the quarks and leptons are made by adding an "s" to the SM name, standing for scalar. Accordingly, the gauge bosons related to the generator of the group $SU(3)_c \otimes SU(2)_L \otimes U(1)_Y$ should also have a spin 1/2 partner, whose name will be made by adding a "ino" at the end of the SM name. The symbol of superpartners is defined by adding a (˜) to the SM symbol. The SUSY particles share the same couplings with their SM partner, since the left-handed and right-handed components of fermions transform differently under gauge transformations also their superpartner present this feature.

The Minimal Supersymmetric extension of the Standard Model (MSSM) [36–41], is defined by requiring the minimal gauge group (i.e., the SM one) and the minimal particle content: three generation of fermions (without right-handed neutrinos), gauge bosons and two Higgs doublet, each with its superpartner. Tables 1.1 and 1.2 summarize chiral and gauge supermultiplets in the MSSM. Among the gauge eigenstates summarized in the tables, the superpartner of the Higgs bosons, the *higgsinos* mix with the *wino* and *bino* to give the "ino" mass eigenstates: two charginos $\chi_{1,2}^\pm$ and four neutralinos $\chi_{1,2,3,4}^0$.

R-parity conservation

The MSSM requires a discrete and multiplicative symmetry called R-parity [35], this symmetry assures barion and lepton number conservation and it is defined as follows:

$$R_p = (-1)^{2s+3B=L} \tag{1.2}$$

where L and B are lepton and barion numbers and s stands for the spin quantum number. The R-parity quantum number has value $+1$ for ordinary SM particles and -1 for their superpartners. This symmetry was first introduced as a simple way to overcome the problem of instability of the proton, lepton and barion number violation leads, in many cases, to unstable proton with life-time shorter than the experimental lower limit. The conservation of R-parity has also other important fenomenological consequences: SUSY particles are always produced in pairs and decays always in an odd number of SUSY particles. Furthermore, the lightest SUSY particle, often chosen as one of the neutralinos, is stable and provides a suitable candidate for dark matter.

Names	Supermultiplets	Spin 1/2	Spin 0
quark, squarks	Q	$(u_L \ d_L)$	$(\tilde{u}_L \ \tilde{d}_L)$
($\times$ 3 families)	$\bar{u}$	$u_R^\dagger$	$\tilde{u}_R^*$
	$\bar{d}$	$d_R^\dagger$	$\tilde{d}_R^*$
leptons, sleptons	L	$(\nu \ e_L)$	$(\tilde{\nu} \ \tilde{e}_L)$
($\times$ 3 families)	$\bar{e}$	$e_R^\dagger$	$\tilde{e}_R^*$
higgsinos, Higgs	H_1	$(\tilde{H}_1^0 \ \tilde{H}_1^-)$	$(H_1^0 \ H_1^-)$
	H_1	$(\tilde{H}_2^+ \ \tilde{H}_2^0)$	$(H_2^+ \ H_2^0)$

Table 1.1: This table is based on Ref. [2] and summarize the chiral supermultiplets in the Minimal Supersymmetric Standard Model. The spin-0 fields are complex scalars and the spin-1/2 are left-handed two-component Weyl fermions.

Names	Supermultiplets	Spin 1	Spin 1/2
gluons, gluinos	G_a (a =1,...,8)	g	$\tilde{g}$
W bosons, winos	W_a (a=1,...,3)	$W^\pm \ W^0$	$\tilde{W}^\pm \ \tilde{W}^0$
B boson, bino	B	B^0	$\tilde{B}^0$

Table 1.2: This table is based on Ref. [2] and summarize the gauge supermultiplets in the Minimal Supersymmetric Standard Model.

The Soft SUSY Breaking

In case Supersymmetry is an exact symmetry of nature, the SM particles and their relative superpartners should have the same mass and quantum numbers, except for the spin. However, the particle spectrum of SUSY has not yet been observed, suggesting that, if these particles exist, they should have an higher mass than their SM superpartners. To achieve SUSY-breaking in a way which does not reintroduce the quadratic divergences to the Higgs mass squared, a so called "soft-SUSY-breaking" term is introduced to the SUSY lagrangian [42,43], this term explicitly break SUSY introducing the mass terms for Higgs, gauginos and sfermions, as well as trilinear coupling terms between sfermions and Higgs bosons. In general, if intergenerational mixing and complex phases are allowed, the soft-SUSY-breaking terms will introduce a huge number of unknown parameters $\mathcal{O}(100)$ [44]. However, in absence of phases and mixing, and if the soft terms obey a set of boundary conditions [42,43], only few new parameters are introduced $\mathcal{O}(10)$.

1.2.2 The Higgs Sector in the MSSM

In the MSSM two doublets of complex scalar field of opposite hypercharge are required to break the electroweak symmetry, this requirement is necessary to generate masses separately for isospin up-type fermion and down-type fermions [34, 45, 46] and to cancel chiral anomalies that otherwise would spoil the renormalizability of the theory [47]. The two Higgs doublet are:

$$H_1 = \begin{pmatrix} H_1^0 \\ H_1^- \end{pmatrix} \text{ with } Y_{H_1} = -1, \qquad H_2 = \begin{pmatrix} H_2^+ \\ H_2^0 \end{pmatrix} \text{ with } Y_{H_2} = +1 \qquad (1.3)$$

In analogy with the SM, a similar Higgs mechanism is employed in the MSSM [36,48] requiring that the minimum of the Higgs potential breaks $SU(2)_L \otimes U(1)_Y$ group while preserving the electromagnetic symmetry $U(1)_Q$. The neutral components of the two Higgs field acquire vacuum expectation values:

$$\langle H_1^0 \rangle = \frac{v_1}{\sqrt{2}}, \qquad \langle H_2^0 \rangle = \frac{v_2}{\sqrt{2}} \qquad (1.4)$$

Three of the original eight degrees of freedom of the scalar fields are absorbed by the $W^\pm$ and Z bosons, which acquire their longitudinal polarizations and masses. The remaning degrees of freedom correspond to five scalar Higgs bosons: two CP-even and neutral h and H, a neutral CP-odd boson A and a pair of charged bosons $H^\pm$. Six parameters describes the MSSM Higgs sector: M_h, M_H, M_A, $M_{H^\pm}$, β and α, where the latter represents the mixing angle in the neutral CP-even sector, while $\tan\beta$ is equal to the ratio between the two vacuum expectation values $\tan\beta = v_1/v_2$. At tree level, only two of these parameters are actually independent, a common choice is to keep $\tan\beta$ and M_A as free the parameters of the Higgs sector. At tree level, the supersymmetric structure of the theory impose a strong hierarchical structure on the Higgs bosons mass spectrum: the h boson is the lightest with $M_h < M_Z$, while $M_A < M_H$ and $M_{H^\pm}^2 = M_A^2 M_W^2$. Furthermore, the following
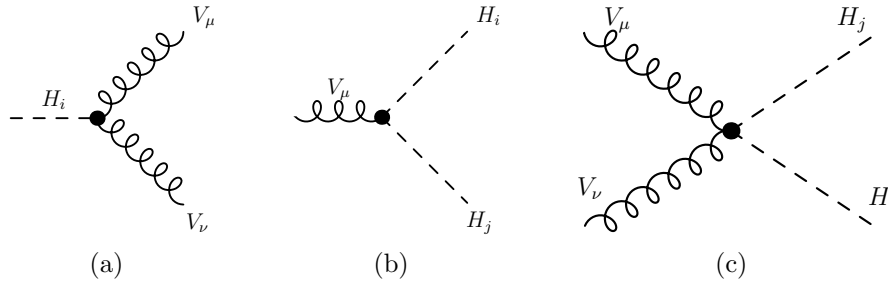
Figure 1.1: Feynman diagrams for the couplings between one Higgs boson and two gauge bosons (a), two Higgs bosons and one gauge boson (b) and two Higgs bosons and two gauge bosons (c). Based on [3].

relation holds between the mixing angles:

$$\cos^2(\beta - \alpha) = \frac{M_h^2(M_Z^2 - M_h^2)}{M_A^2(M_H^2 - M_h^2)} \tag{1.5}$$

These relations are broken by large radiative corrections to the Higgs bosons masses [49], which cause the costraint on the mass of h to move from the tree level value of M_Z to $M_h \lesssim 140$ GeV. Another restriction, coming from GUT assumptions gives $1 \lesssim \tan\beta \lesssim m_t/m_b$ [50].

1.3 Neutral Higgs Bosons Phenomenology in the MSSM

1.3.1 MSSM Higgs Couplings with SM Particles

The phenomenology of the MSSM Higgs bosons depends on their couplings with standard model and supersymmetric particles, a short overview of the former, based on the Ref. [3], is given in this section.

The possible couplings between MSSM Higgs bosons and vector bosons are: the threelinear couplings $V_\mu V_\nu H_i$ among one Higgs boson and two gauge bosons and $V_\mu H_i H_j$ among one gauge boson and two Higgs bosons, as well as the couplings between two Higgs bosons and two gauge bosons $V_\mu V_\nu H_i H_j$. Figure 1.3.1 shows the Feynman diagram relative to these couplings. Among all of them, the most relevat for MSSM Higgs phenomenology is the trilinear couplings between two gauge bosons and one Higgs boson $V_\mu V_\nu H_i$. For this case, since the photon is massless, there are no Higgs-$\gamma\gamma$ and Higgs-$Z\gamma$ couplings at tree level, CP-invariance also forbids WWA, ZZA and $WZH^\pm$ couplings. Then, in case of $V_\mu V_\nu H_i$ couplings, only the following possibilities remains:

$$Z_\mu Z_\nu h \ : \ ig_z M_Z \sin(\beta - \alpha)g_{\mu\nu}, \qquad Z_\mu Z_\nu H \ : \ ig_z M_Z \cos(\beta - \alpha)g_{\mu\nu} \tag{1.6}$$
$$W_\mu^+ W_\nu^- h \ : \ ig_w M_W \sin(\beta - \alpha)g_{\mu\nu}, \quad W_\mu^+ W_\nu^- H \ : \ ig_w M_W \cos(\beta - \alpha)g_{\mu\nu} \tag{1.7}$$

The couplings of the neutral CP-even Higgs bosons h and H with pair of vector bosons are prortional to $\sin(\beta - \alpha)$ and $\cos(\beta - \alpha)$ respectively, where $\cos(\beta -$

α) is fixed at tree level following equation (1.5). An interesting fenomenological consequence is that, calling G_{VVh} and G_{VVH} the coupling between two generic vector bosons and one of the neutral CP-even Higgs bosons the following equation holds:

$$G_{VVh}^2 + G_{VVH}^2 = g_{VVH_{SM}}^2 \qquad (1.8)$$

The equations (1.7) and (1.8) leads to the fact that the couplings with vector bosons for h (H) increase (decrease) with $\tan\beta$. For relatively large value of $\tan\beta$, h has SM-like couplings with vector bosons while H decouple from them. For an overview of all the other couplings between vector bosons and Higgs bosons, charged Higgs, trilinear and quartic coupling between Higgs bosons and couplings to SUSY particles refer to Ref. [3].

The MSSM Higgs bosons couplings with isospin up-type u, and down-type d fermions also depend on $\tan\beta$ and may be written as follows:

$$
\begin{aligned}
G_{huu} &\propto m_u[\sin(\beta-\alpha)+\cot\beta\cos(\beta-\alpha)], & G_{hdd} &\propto m_u[\sin(\beta-\alpha)-\tan\beta\cos(\beta-\alpha)] \\
G_{Huu} &\propto m_u[\cos(\beta-\alpha)-\cot\beta\sin(\beta-\alpha)], & G_{Hdd} &\propto m_d[\cos(\beta-\alpha)+\tan\beta\sin(\beta-\alpha)] \\
G_{Auu} &\propto m_u\cot\beta, & G_{Add} &\propto m_d\tan\beta
\end{aligned}
$$

The couplings with down-type (up-type) fermions of either the h or H boson is enhanced (suppressed) by a factor $\tan\beta$, depending on the magnitude of $\cos(\beta-\alpha)$ or $\sin(\beta-\alpha)$, while the coupling of A boson with down-type (up-type) fermions are directly enhanced (suppressed) by $\tan\beta$.

1.3.2   MSSM Higgs Benchmark Scenarios

At tree level, the MSSM Higgs bosons masses, decay branching fraction and production cross section are all determined by two parameters, by convention chosen to be M_A and $\tan\beta$. As it has been pointed out in Section 1.2.2, radiative corrections contribute significantly to the MSSM Higgs bosons masses and the prediction of physics observables becomes dependent on several MSSM parameters. The main corrections arises from the top-stop (s)quark sector and for large $\tan\beta$ also the bottom-sbottom (s)quark sector becomes increasingly important. Furthermore, these corrections are dependent on the SUSY-breaking scale M_{SUSY}, the trilinear Higgs-stop, Higgs-sbottom Yukawa couplings, the electroweak gaugino and gluino mass parameters.

Due to the large number of free parameters, a complete scan of the MSSM parameter space is impractical in experimental analysis and phenomenological studies. To cope with this difficulty several benchmark scenarios has been proposed [4, 52], where the SUSY parameters entering via radiative corrections are fixed to particular benchmark values which exibit interesting features of the MSSM Higgs phenomenology, while the parameters M_A and $\tan\beta$ are left free to vary. Usually results are presented in a $M_A - \tan\beta$ plane.

The m_h^{max} benchmark scenario [51] was used in the past searches for neutral MSSM Higgs bosons performed at LEP, Tevatron and LHC [64–67]. In this benchmark scenario the parameters that contributes to radiative corrections are fixed such that the mass of the light CP-even Higgs boson, M_h, is maximal under the

variation of M_A and $\tan\beta$. The m_h^{max} scenario allows to set conservative lower bounds on M_A, $M_H^\pm$ and $\tan\beta$ [52]. However, given the recent discovery of a Higgs boson with mass ~ 126 GeV, this scenario tend to predict a too high mass for M_h, resulting to be, for large part of the MSSM parameter space, inconsistent with this observation. This scenario is still currently used in the presented analysis since it offer the possibility to compare results with past experiments.

Recently, several benchmark scenarios has been updated [4] to accommodate the experimental constraints on past neutral MSSM Higgs searches and the observation of a SM-like Higgs boson. An interesting updated benchmark scenario is the m_h^{mod} scenario, which has the feature to predict $M_h \simeq 125.5 \pm 3$ GeV for large region of MSSM parameter space. The m_h^{mod} scenario configuration is obtained by reducing the amount of mixing in the stop sector with respect to the m_h^{max} scenario. This can be done for both signs of the MSSM parameter that regulate the stop mixing X_t, giving rise to two complementary scenarios m_h^{mod+} and m_h^{mod-}. The difference between these two scenarios is found to be negligible for experimental searches, the m_h^{mod+} benchmark scenario has been used throughout this thesis as reference scenario.

Other interesting benchmark scenario are the light stop scenario and the light stau scenatio. The first may lead to relevant modification of the gluon fusion production cross section, while the second leads to modification of the di-photon decay branching fraction of the light CP-even MSSM Higgs boson. For an overview of other relevant benchmark scenarios refer to Ref. [4].

1.3.3 Neutral MSSM Higgs Bosons Production and Decay at LHC

For large region of the MSSM parameter space a SM-like Higgs boson is expected, this role is commonly played by the lightest CP-even Higgs boson, h. Given the Higgs bosons couplings discussed in Section 1.3.1 tourns out that the MSSM Higgs bosons H and A tend to be degenerate in mass and decouple from gauge bosons. Furthermore the coupling of the latter two Higgs bosons with down (up) type fermions are enhanced (suppressed) by $\tan\beta$, therefore, for large $\tan\beta$ bottom-quark and τ lepton will play an important role for the Higgs bosons production and its decays.

The production of the neutral CP-even MSSM Higgs bosons at hadron colliders proceeds via the same processes as for the SM Higgs production. The pseudoscalar A, instead, cannot be produced in association with gauge bosons or in vector boson fusion (VBF) processes at tree-level, as this coupling is forbidden due to CP-invariance. At the LHC one of the most relevant production mechanisms for the MSSM Higgs bosons is gluon fusion, $gg \rightarrow A/H/h$. In addition, the production in association with b-quarks becomes important for large value of $\tan\beta$. These are the only two production mechanism that are considered in the presented analysis. Figure 1.2 shows the Feynman-diagram for these processes, while Figure 1.3 shows the production cross section of the neutral MSSM Higgses via these two processes in the m_h^{max} scenario.

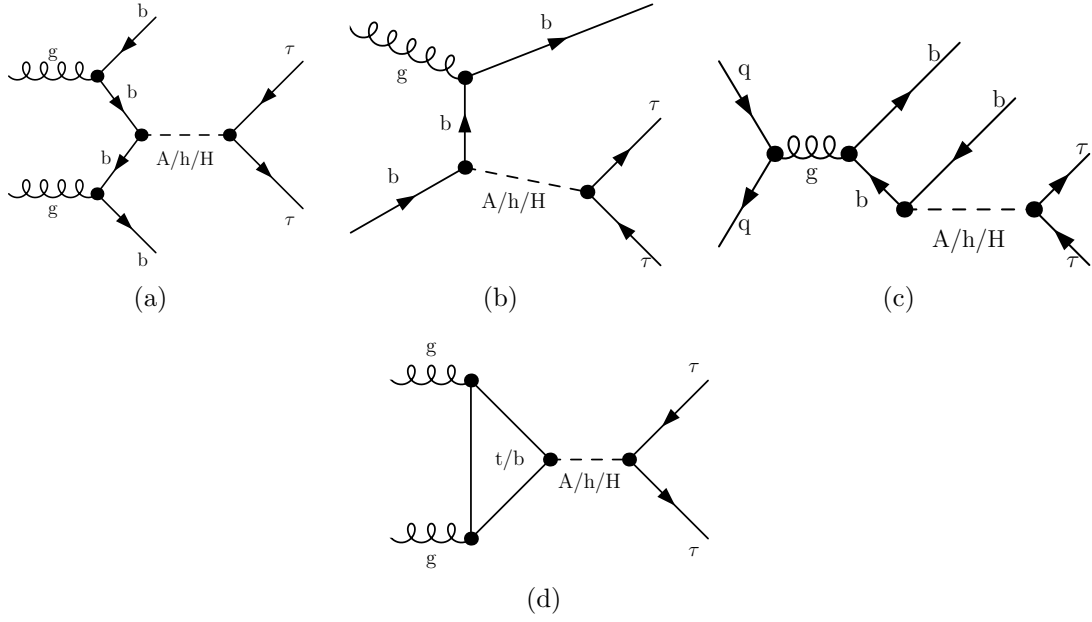The decays of the neutral MSSM Higgs bosons (in the assumption that all

Figure 1.2: Feynman diagram for the production of the neutral MSSM Higgs bosons in association with b-quarks (a,b,c) and via gluon fusion (d) process, subsequent decay in tau lepton pairs is considered.

supersymmetric particle are heavy enough) are the same as for the SM one with the already cited exception of A. Figure 1.3 shows the decay branching fractions in the m_h^{mod+} scenario for h, H and A as a function of the mass of A for two values of $\tan\beta$. The decay into tau lepton pairs is the most important after $b\bar{b}$ and the one used in this thesis.

1.3.4   Current Status of the Searh for Neutral MSSM Higgs Bosons

The measure of the couplings of the observed SM-like Higgs boson can shed light on the Higgs sector and determine if this boson is fully responsable for the generation of all the SM particles masses. There are two approaches to explore the Higgs sector: one, is to use the measured Higgs couplings with SM particles to set constraint on new physics, while the other is to directly search for additional Higgses in a well defined model.

In case the SM-like Higgs boson is interpreted as the light CP-even Higgs boson of the MSSM, the couplings of the Higgs boson to vector bosons (k_V), up-type fermions (k_u) and down-type fermions (k_d), can be expressed as a function of m_A and $\tan\beta$ and this allow to set exclusion limits in the $m_A - \tan\beta$ plane [53]. Figure 1.5 shows the exclusion limits in a "simplified MSSM" model [54, 55] via fits to the measured rates of Higgs boson production and decay.

The current latest constraint on $m_A - \tan\beta$ by direct search of neutral MSSM Higgs bosons [] are instead shown in Figure 1.6 and are part of the work of this thesis.
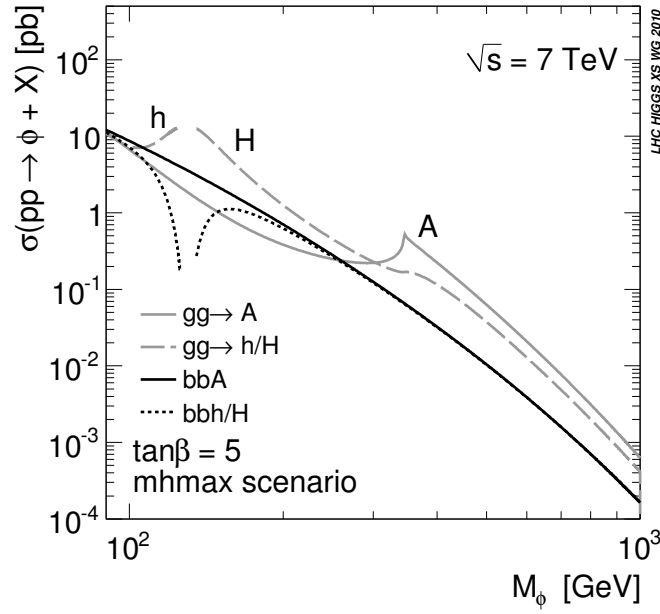
(a)
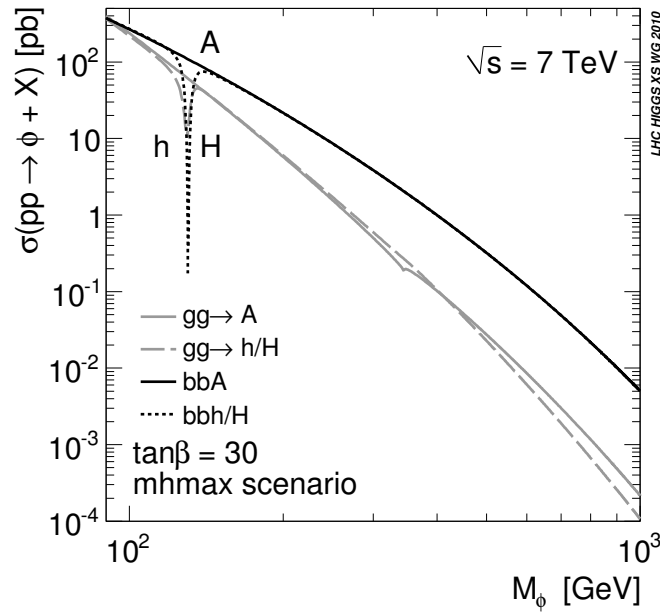
(b)

Figure 1.3: Central predictions for the total MSSM Higgs bosons production cross sections via gluon fusion and Higgs radiation off bottom quarks for $\sqrt{s} = 7$ TeV using NNLO and NLO MSTW2008 PDFs m_h^{max} scenario; (a) $\tan\beta = 5$, (b) $\tan\beta = 30$. Ref. [5].
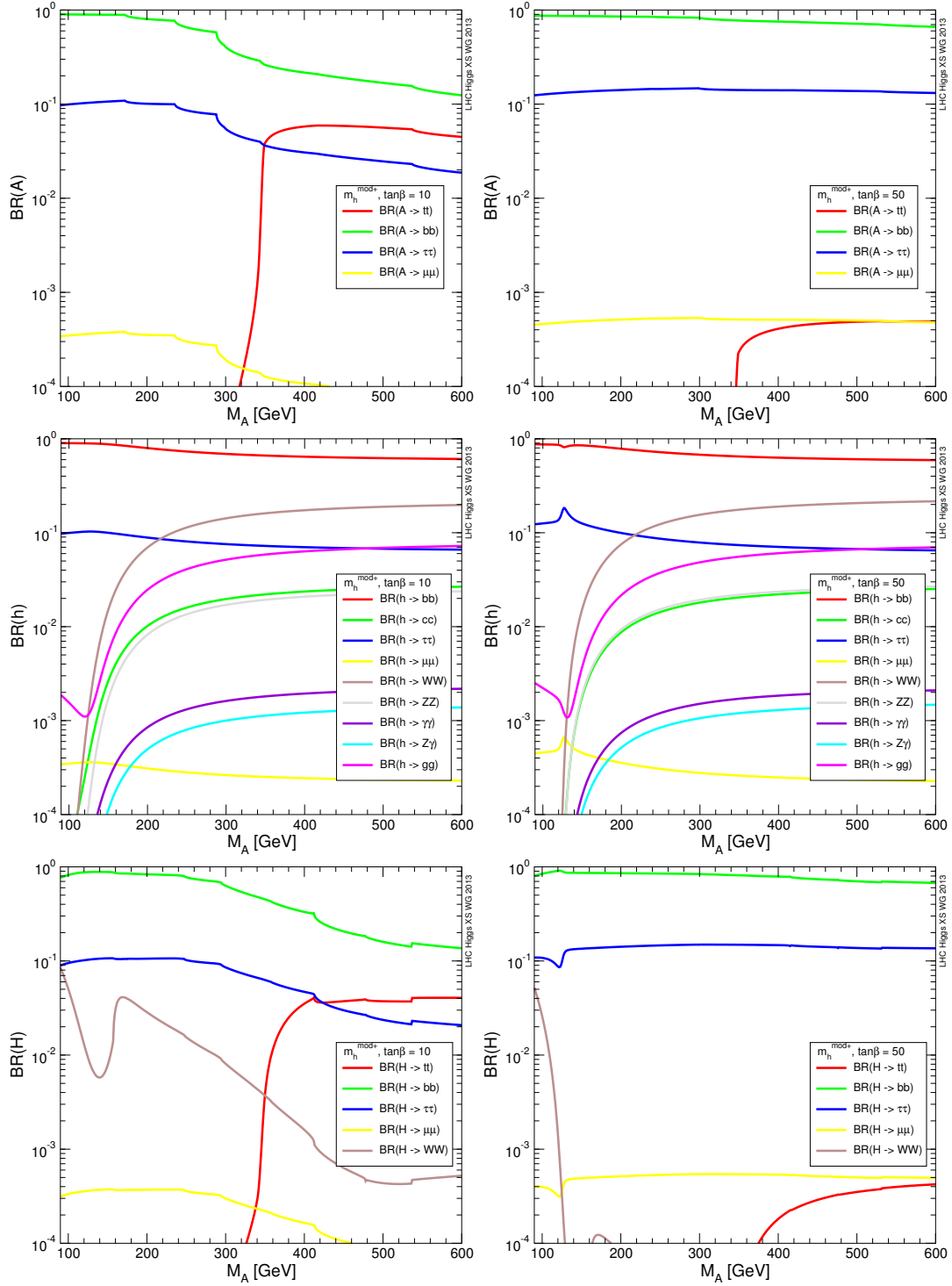
Figure 1.4: Branching fraction for the MSSM neutral higgses $h/H/A$ in the m_h^{mod+} scenario for $\tan\beta = 10$ and $\tan\beta = 50$. Ref. [4].
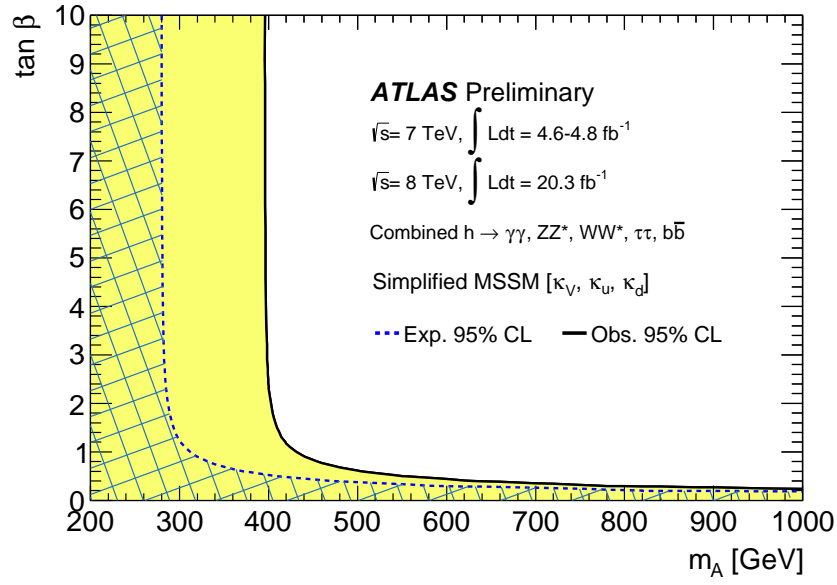
Figure 1.5: Regions of the $m_A - \tan\beta$ plane excluded in a simplified MSSM model via fits to the measured approximately to 95% CL (2σ), are indicated for the data and expectation assuming the SM Higgs sector. The light shaded and hashed regions indicate the observed and expected exclusions, respectively. The SM decoupling limit is $m_A \to \infty$. See Reference [53].
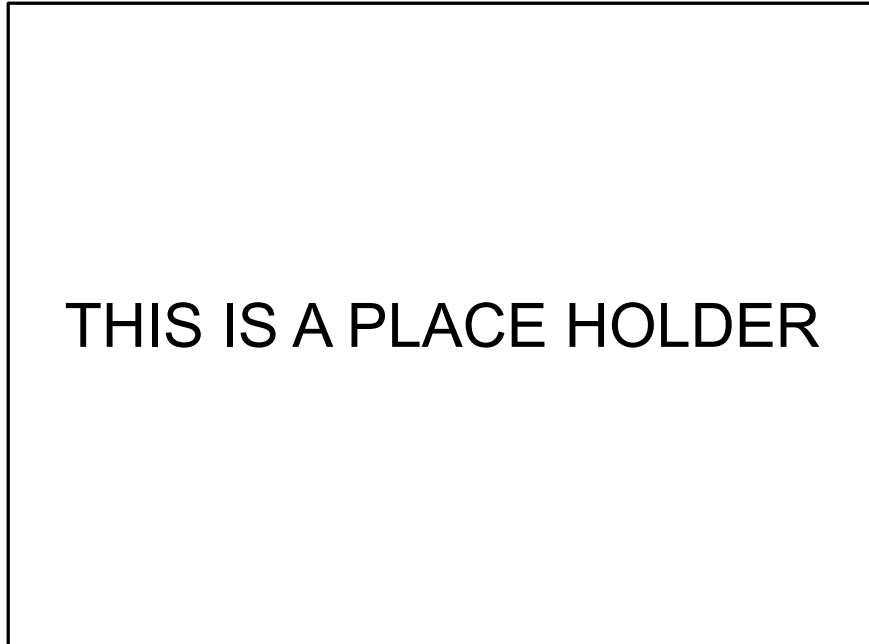
Figure 1.6: Limit CMS or ATLAS depending if we manage to publish in time

Chapter 2

The ATLAS Detector at the LHC

The Large Hadron Collider (LHC) located at the European Organization for Nuclear Research (CERN) is the largest particle collider facility in the world. The ATLAS experiment is one of the several experiment situated at the LHC, it is a general-purpose detector dedicated to explore a wide range of physiscs topics, from precision measurements of known Standard Model processes to the search for physics beyond the Standard Model. Proton-proton collision data recorded by the ATLAS experiment has been used in this thesis for the search for the neutral MSSM Higgs bosons.

This chapter is organized as follows: the design and performance of the LHC are summarized in Section 2.1 (based on Ref. [56]), while a description of the ATLAS detector is given in Section 2.2 (based on Ref. [57]).

2.1 The Large Hadron Collider

The LHC is a superconducting hadron syncrotron collider. It is installed in the tunnel of the former LEP electron-positron collider and has ~ 27 km circumference. LHC is designed to collide proton beams with a centre-of-mass energy of 14 TeV and an unprecedented luminosity of $10^{34}\ cm^{-2}s^{-1}$. It can also collide heavy ions (lead) with an energy of 2.8 TeV per nucleon and a peak luminosity of $10^{27}\ cm^{-2}s^{-1}$.

The LHC provides proton-proton collision for several experiments, the most relevant for the physics program are the ATLAS, CMS [59], LHCb [60] and ALICE [61] experiments. Figure 2.1 shows the layout of the CERN accelerator complex, the protons follows several acceleration steps before injection in the LHC machine. First a linac accelerator (*Linac* 2) accelerates the protons to an energy of 50 MeV, then they are injected in the *booster* which accelerates them further to 1.4 GeV. The energy is increased to 25 GeV and successively to 450 GeV by means of two syncrotron accelerators, the *Proton Syncrotron* (PS) and the *Super Proton Synctrotron* (SPS). Finally, two proton beams are injected with opposite direction into the LHC where they reach their final erergy.

The LHC beams are costituited by bunches of protons which are housed in two separate vacuum pipes. Radiofrequency cavities are employed to accelerate the protons, while superconductig magnets bends and focuses the bunches. The LHC is designed to accelerate up to 2835 bunches per beam, each of them containing $\sim 10^{11}$ protons. The nominal bunch spacing allows collision every 25 ns representing a real challenge for any read-out electronics.

In 2010, fist collisions took place at the LHC between proton beams of energy of 3.5 TeV. The LHC was succesfully in operation during years 2011 and 2012, beam of protons were initially delivered with energies of 3.5 TeV which was increased to 4 TeV in 2012. Peak luminosities of about $4 \times 10^{33}\ cm^{-2}s^{-2}$ and $8 \times 10^{33}\ cm^{-2}s^{-2}$ have been reached during years 2011 and 2012 respectively. The ATLAS experiment recorded in fully operational conditions an integrated luminosity of 4.57 fb^{-1} during year 2011, while an integrated luminosity of 20.3 fb^{-1} was recorded during year 2012. Data recordered during these two years led to one of the major mailstone in particle physics, the discovery in 2012 of a Higgs boson.

2.2 The ATLAS Detector

The ATLAS detector is a multi-purpose detector which aim to explore a wide range of physiscs topics. The physics programme of the ATLAS experiment ranges from precision measurements of known Standard Model processes to the search for physics beyond the Standard Model in a large variety of scenarios. The ATLAS detector is designed to satisfy the tight requirements on particle identification and acuracy imposed by the physics goals. A schematic view of the ATLAS detector is shown in Figure 2.2. ATLAS is $44\,m$ long and $25\,m$ high, it has a typical design for a collider experiments with a forward-backward symmetry with respect the interaction point. It consist of four sub-detector which are built cylindrically around the beam pipe, going from the inside to outside they are: an Inner Detector tracker, an electromagnetic calorimeter, an hadronic calorimeter and finally a muon spectrometer
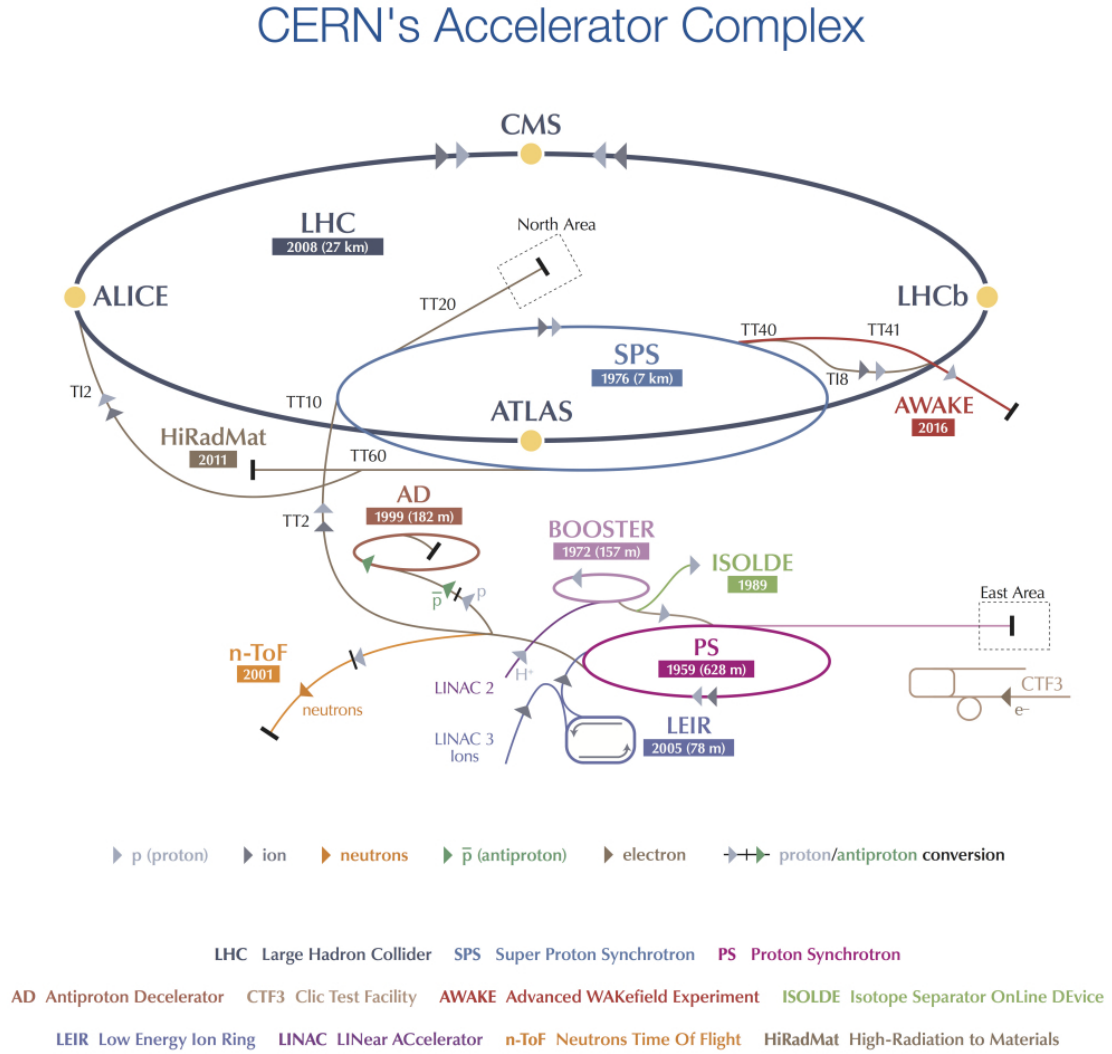
Figure 2.1: Illustration of the CERN accelerator complex [58]. The acceleration of protons starts with Linac2 followed by the acceleration in the Booster. The Proton Syncrotron (PS) and the Super Proton Syncrotron (SPS) accelerate further the protons before final injection into the LHC machine.
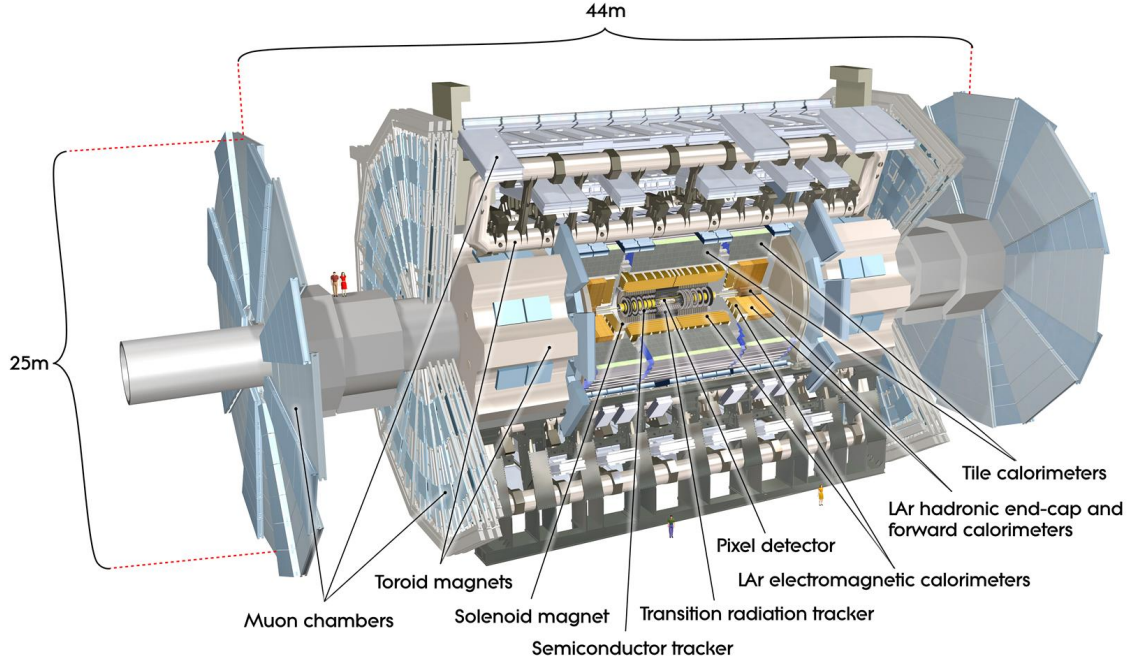
Figure 2.2: Cut-away view of the ATLAS detector with its sub-detectors system. Ref. [57].

sourrounds the whole experiment. Each of these sub-detector is briefly described in what follows based on Ref. [57].

2.2.1   The ATLAS coordinate system

The ATLAS coordinate system has its origin in the interaction region. The $z-$axis is pointing along the beam direction, the $y-$axis is pointing upwards and the $x-$axis towards the center of the LHC ring. The angle ϕ is defined in the plane orthogonal to the beam axis, starting from the positve side of the $x-$axis. The angle θ is instead defined with respect to the $z-$axis. A commonly used spatial coordinate in experiments at collider is the rapidity y:

$$y \; = \; 1/2 \cdot \ln\left(\frac{E + p_z}{E - P_z}\right) \tag{2.1}$$

The difference in the rapidity of two particles is independent of Lorentz boosts along the beam axis. In the limit of β approaching to one or for massless particle the rapidity tend to the pseudorapidity η:

$$\eta \; = \; 1/2 \cdot \ln\left(\frac{\theta}{2}\right) \tag{2.2}$$

Given the symmetry of the ATLAS detector with respect to the interaction point, the detector is divided in two regions called *barrel* for $|\eta| \lesssim 1.5$ (depending on the

Figure 2.3: Cut-away view of the ATLAS Inner Detector tracker. Ref. [57].

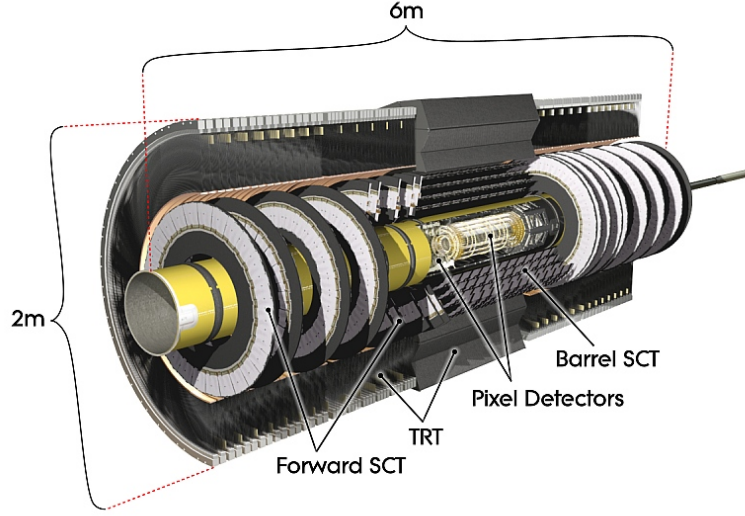considered detector) and *endcap* for larger η. In ATLAS the angular separation between two particle is commonly measured by $\Delta R = \sqrt{\Delta \eta^2 + \Delta \phi^2}$.

2.2.2 The Inner Detector

The Inner Detector (ID) performs track reconstruction and momentum measurements of charged particles, it has a total lenght of $5.3\,m$ and a diameter of $2.5\,m$. The momentum measurment is performed by measuring the tracks curvature in a $2\,T$ magnetic field generated by a super-conducting solenoid. The layout of the Inner Detector is illustrated in Figure 2.3, it consist of three independent detector modules with fine granularity covering the region $|\eta| < 2.5$. The innermost of these detectors is the Pixel detector, which consist of three cylindrical layers of pixel silicon sensors in the barrel and three disks in the endcap region. The closest layer of pixels to the beam pipe is referred to as the B-layer. The spatial resolution of the pixel sensors is $10\,\mu m$ in the transverse and $115\,\mu m$ in the longitudinal direction with respect to the beam pipe.

The Semi-Conductor Tracker (SCT) surrounds the Pixel detector with four cilindrical layers of silicon microstrip sensor in the barrel and nine disks in the endcap region. The spatial resolution achieved by the SCT is of $17\,\mu m$ in the transverse and $590\,\mu m$ in the longitudinal direction respectively.

The outermost detector module is the Transition Radiation Tracker (TRT). It is composed of $4\,mm$ diameter Kapton straw tubes with a tungsten wire in their center. The tube is filled with a gas mixture which allows the detection of transition radiation photons. This detector can only measure position along the transverse direction.
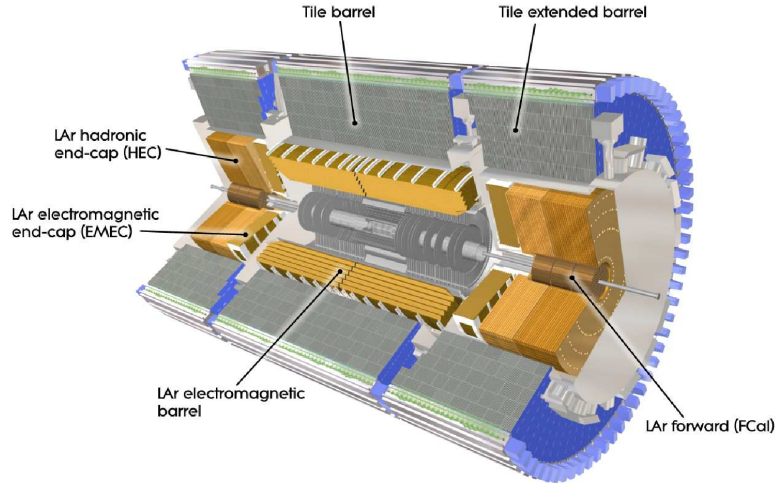
Figure 2.4: Cut-away view of the ATLAS calorimeter system. Ref. [57].

2.2.3   The Calorimeter System

An illustration of the ATLAS calorimeter system is shown in Figure 2.4, it consist of an electromagnetic calorimeter (EM) sourraunded by an hadronic calorimeter. These calorimeters cover the range $|\eta| < 4.9$ using different techniques suited to the widely varying radiation environment over this large $\eta-$range. Both these calorimeters are sampling calorimeters, they are builded alternatig active material, which performs the detector response and a passive absorber. The total detector thickness at $\eta = 0$ is 9.7 interaction lenght.

The EM Lar calorimeter is ideally suited for precision measurements of electrons and photons. It uses lead as absorber material and liquid argon as active material. It extends up to $|\eta| < 3.2$.

The hadronic calorimeter has a coarser granularity with respect the EM calorimeter and it is suited for jet reconstruction and E_T^{miss} measurements. The hadronic calorimeter is divided in three sub-detectors which make use of different technology to cope with the changing radiation environment as a function of η. The Tile calorimeter covers region in pseudorapidity up to $|\eta| < 1.7$, it uses scintillating tiles as active material and steel as absorber. In the forward region ATLAS is instrumented with a Lar hadronic endcap calorimeter (HEC), which extends up to $|\eta| < 3.2$ and uses argon as active material and copper as absorber. The region in $3.1 < |\eta| < 4.9$ is istrumented instead with a liquid argon Forward CALorimeter (FCAL), which is divided in three modules, the closest to the interaction point uses copper as absormer material, while the other two uses tungsten.

2.2.4   The Muon Spectrometer

The muon spectrometer is instrumented with separate high-precision tracking and trigger chambers. The measure of muon momenta is performed by reconstructing the track curvature in an intense magnetic field produced by the large supercon-
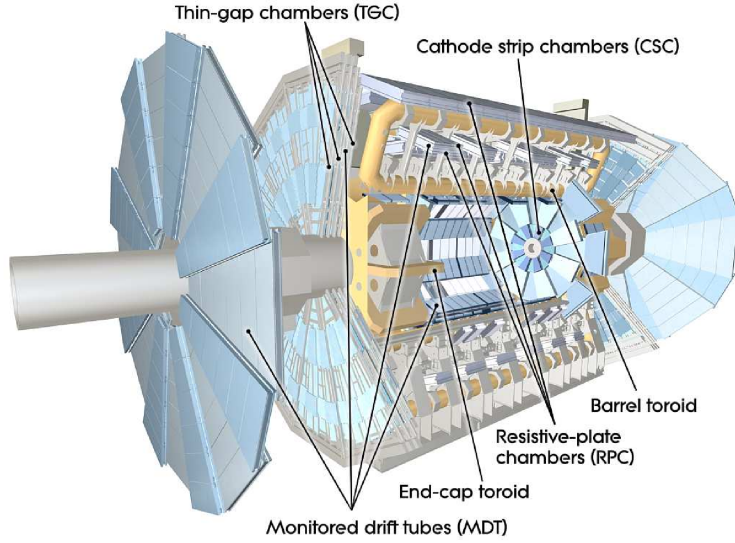
Figure 2.5: Cut-away view of the ATLAS muon spectrometer system. Ref. [57].

ducting air-core toroid magnets. The layout of the muon spectrometer is shown in Figure 2.5.

Precision measurement of the track coordinates in the principal bending direction of the magnetic field is provided by Monitored Drift Tubes (MDTs) up to $|\eta| < 2.7$. Given the demanding rate and background conditions at large pseudorapidities, $2 < |\eta| < 2.7$, the innermost MDT layer is replaced by Cathode Strip Chambers (CSCs), which are multiwire proportional chambers with cathodes segmented into strips. Precise muon momentum measurement is achieved for muons with momenta up to 1 TeV. The best momentum resolution, 3-4%, is achieved for muons with transverse momenta ~ 100 GeV, while resolution of $\sim 10\%$ are reached for muons with momenta up to 1 TeV.

The trigger system covers the pseudorapidity range $|\eta| < 2.4$. Resistive Plate Chambers (RPCs) are used in the barrel and Thin Gap Chambers (TGCs) in the end-cap regions for the trigger information.

2.2.5 The Trigger System

The trigger system has three distinct levels: L1, L2, and the event filter (EF). Each trigger level refines the decisions made at the previous level and, where necessary, applies additional selection criteria.

The L1 trigger searches for high transverse-momentum muons, electrons, photons, jets, and τ leptons decaying into hadrons, as well as large missing and total transverse energy. Its selection is based on information from the set of detectors described previously. The L1 trigger defines in the interesting events one or more Regions-of-Interest (RoI), given by $\eta - \phi$ coordinates of interesting feature of the event.

The L2 selection is seeded by the RoI information provided by the L1 trigger,

it uses the full granularity and precision of all the available detector data within the RoIs. The L2 triggers are designed to reduce the trigger rate to approximately 3.5 kHz.

The final stage of the event selection is carried out by the event filter, which reduces the event rate to roughly 200 Hz. Its selections are implemented using offline analysis and reconstruction procedures.

2.2.6 Luminosity Measuremet

A precise measurement of the recordered integrated luminosity is extremely important for all the physics measuremens of the ATLAS physics program.

Several technique are employed in ATLAS for the measure of the luminosity, the most relevant detectors that monitor the luminosity are the Inner Detector, the BMC and the LUCID detectors. For a detailed description of the ATLAS luminosity measurements and their performance see Ref. [63]. The Inner Detector measure the luminosity by the averange reconstructed proton-proton interaction per buch crossing. The LUCID detector surrounds the beampipe on both sides of the interaction point at a distance of 17 m, providing whit its Cherenkov detectors the measures of the particle flux from the interaction point in a very forward region. The BCM counts the number of collision per bunch crossing providing an independent luminosity estimate.

Chapter 3

Search for neutral MSSM Higgs Bosons in $A/h/H \rightarrow \tau^+\tau^- \rightarrow e\mu + 4\nu$ decays

In light of the recent discovery of a Higgs boson with mass of ~ 126 GeV at LHC [16, 17], it remains an open question whether this new particle is the only missing piece of the electroweak symmetry breaking sector or whether it is one of several Higgs bosons predicted in some theories that go beyond the SM. The most recent measurements [125–128] of its properties shows this new boson to be, within experimental uncertainties, fully compatible with the SM Higgs boson. Nevertheles, such a new particle can also still be accommodated within several theories beyond the standard model (BSM), among all of them, Supersymmetry is a theoretically favoured scenario as the most predictive framework beyond the Standard Model.

This chapter presents the search for the neutral MSSM Higgs bosons decaying into pairs of tau leptons in the fully leptonic final state, published in Ref. []^1 as a part of the search for the neutral MSSM Higgs bosons in all final states of the tau leptons decay. The search is based on 20.3 fb^{-1} of 8 TeV data recorded by the ATLAS experiment during 2012 at the Large Hadron Collider. The chapter is organized as follows: a brief summary of the MSSM Higgs sector and an introduction to the analysis strategy is given in Section 3.1, while the event selection and categorization are described in Section 3.2. In Section 3.3 the estimation of the background is described and in Section **??** methods to evaluate sys-

---

^{1}to Sandra: I'll remove this sentence if Conf note wont be ready in time

tematic uncertainties are discussed. Finally, in section **??**, an overview of the statistical methods employed along with the corresponding result of the search are presented.
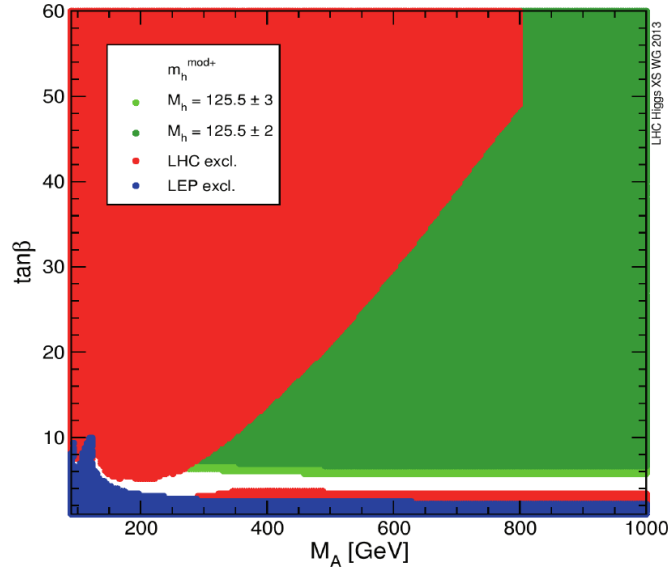
Figure 3.1: Excluded and allowed regions of the $m_A - \tan\beta$ parameter space for the m_h^{mod+} MSSM benchmark scenario. Excluded regions are determined based on direct Higgs boson searches at LEP (blue) and LHC (red). The two green bands correspond to the parameter regions which are compatible with the assumption that the lightest MSSM Higgs boson, h, has a mass respectively of $M_h = 125.5 \pm 2$ (dark green) or 125.5 ± 3 GeV (light green). For more detail see [4].

3.1 Introduction

3.1.1 The Higgs Sector in the MSSM

In the Minimal Supersymmetric extension of the Standard Model (MSSM) [36, 37] the Higgs sector is composed of two Higgs doublets of opposite hyper-charge, resulting in five observable Higgs bosons: two of these are neutral and CP-even (h,H), one is neutral and CP-odd (A) and two are charged ($H^{\pm}$). At tree level their properties such as masses, widths and branching ratios can be predicted in terms of only two parameters, often chosen to be the mass of the CP-odd Higgs boson m_A and the ratio of the vacuum expectation values of the two Higgs doublets $\tan\beta$ (for more details see chapter **??**). The MSSM predicts the existence of a Higgs boson with properties that resemble those of a SM Higgs boson in large regions of its parameter space. This is usually the case for the lightest Higgs boson, h, while the other two, H and A, tend to be degenerate in mass and decouple from gauge bosons. On the other hand, the couplings of the latter two Higgs bosons with down (up) type fermions are enhanced (suppressed) proportionally to the value of $\tan\beta$, meaning that for large $\tan\beta$ bottom-quark and τ lepton will play an important role for the Higgs bosons production and its decays.

The two most relevant MSSM Higgs bosons production mechanisms at the LHC are gluon fusion, $gg \to A/H/h$, and the production in association with b-quarks, $pp \to b(b)A/h/H$, the latter becoming increasingly important for large values of

$\tan\beta$. These two are the only production mechanisms considered in this analysis. Assuming there are no decays into supersymmetric particles since these are too heavy, the favored neutral MSSM Higgs bosons decay mode is the decay into a pair of b-quark and antiquark, $A/h/H \to b\bar{b}$. This is followed, for the CP-odd A and CP-even H Higgs bosons, by the decay into pairs of τ leptons. Given that it is very difficult to distinguish the former decay from the large $b\bar{b}$ background, the decay mode $A/h/H \to \tau^+\tau^-$ provides the highest sensitivity in the search for neutral MSSM Higgs bosons.

Searches for neutral MSSM Higgs bosons have been performed at LEP [64], the Tevatron [65] and the LHC [66,67]. In the following the search for the neutral MSSM Higgs bosons in the final state $A/h/H \to \tau^+\tau^- \to e\mu + 4\nu$ is presented. This search is complementary to the searches in other $\tau^+\tau^-$ final states characterized by the presence of one or two hadronicaly decaying τ leptons. Despite of the fact that the $\tau\tau$ branching ration in $e\mu + 4\nu$ is only 6%, this decay channel provides a sensitivity to the signal comparable to those in other $\tau\tau$ final states, especially for low m_A values. This is mainly due to the high transverse momentum treshold at the trigger level for hadronicaly decaying τ leptons.

As it is impractical for an experimental search to explore the full parameter space of the MSSM, which has many free paramers, several benchmark scenarios are introduced by fixing all except m_A and $\tan\beta$ parameters to values typical for most interesting physics cases. With the recent Higgs boson discovery, benchmark scenarios of the MSSM have been updated to accommodate for new experimental constraints. As an example, Figure 3.1 shows the currently excluded and allowed regions of the MSSM parameter space for the m_h^{mod+} updated benchmark scenario. In this scenario a large region of the $m_A - \tan\beta$ parameter space is compatible with the assumption that the observed Higgs boson correspond to the supersymmetric SM-like Higgs boson, h. A large part of this parameter space is still experimentally unexplored, this is a strong motivation to pursue the search for additional neutral MSSM Higgs bosons.

3.1.2   Signal and Background Processes

Signal events in which the neutral MSSM Higgs bosons decay through $A/h/H \to \tau^+\tau^- \to e\mu + 4\nu$ process are characterized by the presence of one electron and one muon of opposite charge. These two leptons are isolated and have relatively high transverse momenta. In addition, four neutrinos contribute to the missing transverse energy in the event. Figure 3.2 shows leading order Feynman diagram for the two considered signal production modes, gluon fusion and in association with b-quarks. The presence (absence) of a b-jet in the final state serves as a main caracteristic for the event categorization in the latter (former) case, as described later on.

The described signal topology is common to several other known SM background processes which in general have higher cross sections than the sought signal. The dominant background processes are the $Z/\gamma^* \to \tau^+\tau^-$ production either via Drell-Yan process or in association with jets and the top quark production ($t\bar{t}$ and single top quark production). Additional significant background contributions originate
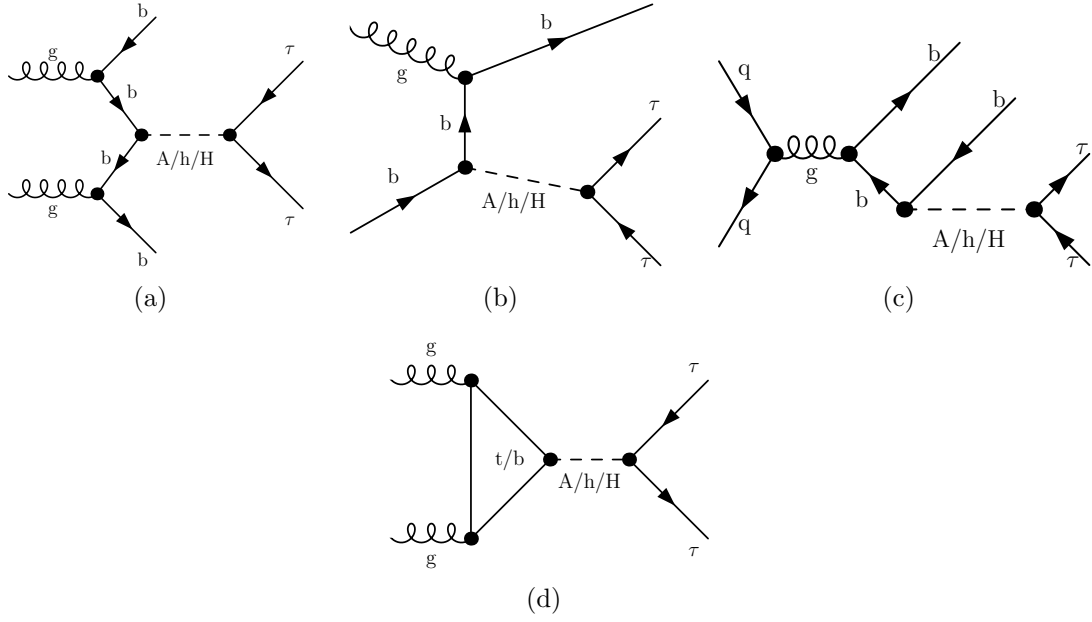
Figure 3.2: Feynman diagram for the production of the neutral MSSM Higgs bosons in association with *b*-quarks (a,b,c) and via gluon fusion (d) process, subsequent decay in tau lepton pairs is considered.

from the dibosons production (WW, WZ, ZZ) and QCD multi-jet events with non-prompt leptons from hadron decay. Vector boson production ($W \rightarrow \ell\nu$ or $Z \rightarrow \ell\ell$, where $\ell \equiv e, \mu$) in association with jets is also considered, but has small impact on the total background contamination. Examples of leading order Feynman diagrams for the dominant background processes are shown in Figure 3.3. The production cross sections times the relevant branching fraction for signal and background processes are summarized in Table 3.1.

3.1.3 Analysis Strategy

In this thesis a search for the MSSM $A/h/H \rightarrow \tau^+\tau^- \rightarrow e\mu + 4\nu$ decays is presented. The $ee + 4\nu$ and $\mu\mu + 4nu$ final states are not considered since a large background background contribution is expected from $Z \rightarrow ee$ and $Z \rightarrow \mu\mu$ decays, respectively, such that the sensitivity of the search in these final state is significantly reduced.

Candidate events are selected based on the topological properties of the Higgs boson production and decay. The presence of exactly one electron and one muon is , isolated and of opposite charge. The set of events is divided in two orthogonal category which are optimized separately for the two different production mode considered. In the gluon-gluon fusion category (also called *b-vetoed* category), the absence of a b-tagged jet is required, the main background in this category is $Z/\gamma^* \rightarrow \tau\tau$. In contrast, the presence of a b-tagged jet is required for b-associated production category (also called *b-tagged* category), the request of a b-jet suppress the $Z/\gamma^* \rightarrow \tau\tau$ background, $t\bar{t}$ and single top production are then the main backgrounds in this category.
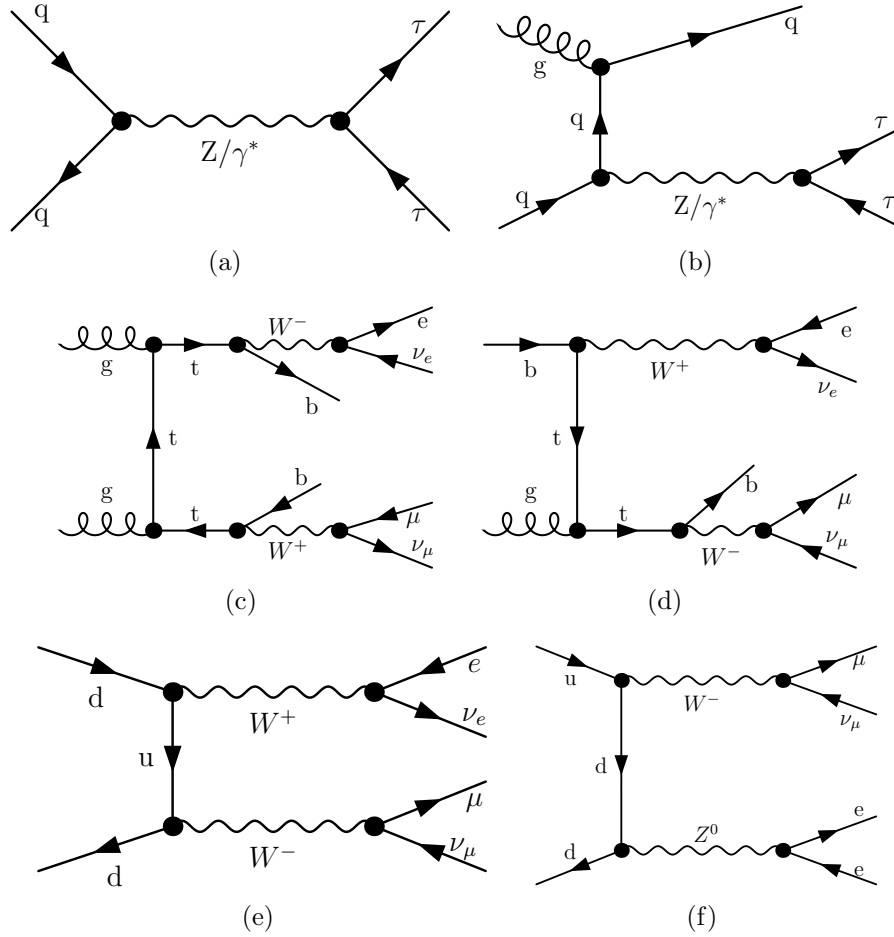
Figure 3.3: Examples of tree level Feynman diagrams for the production and decays of the most relevat backgrounds. The production of $Z/\gamma^* \to \tau^+\tau^-$ either via Drell-Yan process or in association with jets is shown in (a) and (b), top quark pair and single top quark production in (c) and (d), while examples of WW and WZ production are shown in (e) and (f) respectively.

Process	Cross-section (pb) [$\times$ BR]
Signal ($m_A = 150$ GeV, $\tan\beta = 20$, m_h^{max} scenario)	
$gg \rightarrow A/h/H \rightarrow \tau\tau \rightarrow e\mu + 4\nu$)	0.12/0.09/0.13
$pp \rightarrow b\bar{b}A/h/H \rightarrow \tau\tau \rightarrow e\mu + 4\nu$)	0.29/0.03/0.25
Backgrounds	
$W \rightarrow \ell$+jets	12.22×10^3
$Z/\gamma^* \rightarrow \ell\ell$+jets	5.5×10^3
$t\bar{t} \rightarrow \ell\ell + X$	137.3
Single top (t, s and Wt channels) $\rightarrow \ell + X$	28.4, 1.8, 22.4
Dibosons WW, WZ and ZZ $\rightarrow \ell + X$	20.6, 6.8, 1.55

Table 3.1: The cross sections multiplied by the relevant branching ratios (BR) for signal and the considered backgrounds. the symbol ℓ stands for $\ell = (e, \mu, \tau)$. Signal cross sections are calculated for the m_h^{max} scenario shown for $m_A = 150$ GeV and $\tan\beta = 20$, in this case $m_H = 151$ GeV and $m_h = 129$ GeV.

The $A/h/H \rightarrow \tau\tau \rightarrow e\mu + 4\nu$ search is performed in the MSSM m_h^{max} benchmark scenario scanning the $m_A - \tan\beta$ plane in the ranges $90 \leq m_A \leq 300$ GeV and $5 < \tan\beta < 60$, the signal prediction for the event yield and kinematical distributions is evaluated by simulation.

The dominant $Z/\gamma^* \rightarrow \tau\tau$ background is estimated from data via a signal-depleted control sample. The QCD multi-jet background contribution is also estimated from data since it represent a challenge for MC simulation. The estimation of the contribution of all the other backgrounds is obtained by means of MC simulation. The background model predictions are validated using different signal-depleted control data samples, good agreement is found.

The systematics uncertainties taken into account for simulated signal and backgrounds arise from uncertainties on cross section calculations and on the modeling of the detector response. For backgrounds that are estimated from data, specific uncertainty are evaluated considering the possible uncertainties of the estimation methods.

The final statistical interpretation of the data is based on the comparison of the observed invariant mass distributions with the expected background and signal-plus-background predictions. Exclusion limits are set by means of a binned likelihood ratio test statistic. The limits are interpreted in the MSSM m_h^{max} scenario and evaluated as a function of m_A and $\tan\beta$. Furthermore, the limits are interpreted, in a less model depended way, in terms of the cross section for the production of a generic Higgs boson, ϕ, of mass m_ϕ, via the production mode $pp \rightarrow b\bar{b}\phi$ and $gg \rightarrow \phi$.

3.1.4   Data and Simulated Event Samples

Data Sample

The presented result are based on proton-proton collision data collected at the LHC during 2012 at a center-of-mass energy of $\sqrt{s} = 8$ TeV, corresponding to an integrated luminosity of 20.3 fb^{-1}. The events used in this analysis are recorded

using a combination of a single electron and combined electron-muon triggers. Only recorded events in which all the relevant components of the ATLAS detector were fully operational are considered. Additional data quality requirements are applied to the events according to [113], these requirements assures the rejection of events with data corruption due to the LAr and Tile calorimeters and with jet activity in known noisy calorimeter regions.

Signal Samples

Signal production via the gluon fusion process, $gg \to A/H/h$, was simulated with POWHEG [77] and the associated $b\bar{b}A/H/h$ production with SHERPA [78]. The pseudo scalar Higgs boson samples were generated in the mass range from 90 GeV to 300 GeV and at $\tan\beta = 20$, the same kinematics are assumed for $A/h/H$ Higgs bosons decay products and at other $\tan\beta$ values, appropriate re weighting is applied according to the different cross-sections. The $m_h^{\max}$ MSSM benchmark scenario is assumed.

Background Samples

The production of W and Z/γ^* bosons in association with jets was simulated with the ALPGEN [70] generator. The $t\bar{t}$ process was generated using the POWHEG generator. The single-top (s-channel, Wt) processes were generated using MC@NLO [72], while single-top (t-channel) processes were generated with AcerMC [73]. The production of dibosons (WW, WZ, ZZ) were generated with HERWIG [74]. For all ALPGEN and MC@NLO samples described above, the parton shower and hadronisation were simulated with HERWIG and the activity of the underlying event with JIMMY [75]. Different parton density functions (PDFs) sets are used depending on the generator: CTEQ6L1 [79] is used by ALPGEN and AcerMC while CT10 [80] is used by SHERPA, POWHEG and MC@NLO.

TAUOLA [82] and PHOTOS [83] are used to model the tau lepton decay and additional photon radiation from charged leptons in the leading-log approximation, respectively.

The ATLAS detector response is simulated for all the MC samples using GEANT4 [84, 85], the physics object reconstruction is performed with the same software as for data described in chapter **??**. The effects of the simultaneous recording of several events from the same or neighboring bunch crossings (pile-up) are considered in the simulation.

3.2　Event Selections and Categorization

3.2.1　The "Common" Selections

According to the signal events characteristics, each event either data and MC should satisfy the following selection criteria, these selections are shared by both analysis category and therefore referred in the following as "common selections":

(i) A trigger selection, requiring the presence of an electron with $P_T > 24$ GeV, or alternativaley, an electron with $P_T > 12$ GeV togheter with a muon with $P_T > 8$ GeV.

(ii) At least one reconstructed vertex with more that three associated tracks. This selection is aimed to reject background from cosmic muons.

(iii) Exactly one reconstructed "Tight" electron with $|\eta| < 1.37$ or $1.52 < |\eta| < 2.47$. The electron should have $P_T > 15$ or 25 GeV depending on the trigger that selected the event.

(iv) Exactly one "Combined" muon with $|\eta| < 2.5$ and $P_T > 10$ GeV.

(v) The electron should be isolated with $E_T^{cone}/P_T < 0.08$ and $P_T^{cone}/P_T < 0.06$.

(vi) The muon should be isolated with $E_T^{cone}/P_T < 0.04$ and $P_T^{cone}/P_T < 0.06$

(vii) Muon and electron should be of opposite charge.

(viii) Overlap removal between electron, muon, τ_h and jets is performed.

(ix) The events is rejected if at least one hadronic τ decay is found with $P_T > 15$ GeV.

(x) The invariant mass of the sum of the electron and muon 4-vectors should be greather than 30 GeV.

For details about the definition of physics object used above and their quality requirements refer to chapter **??**.

The two analysis category, *b-tagged* and *b-vetoed*, are defined adding on top of the common selections the request of exactly one b-tagged jet or the absence of b-tagged jet in the event respectively. To be *taggable* a jet should have $P_T > 20$ GeV, $|\eta| < 2.5$ and JVF > 0.5. A jet is considered tagged if passes the selection of the $MV1$ algorithm at 70% of efficiency for b-quark, $\epsilon_b^{t\bar{t}}$. Further selection are applied to each category and optimized separately, these additional selection are described in the following.

3.2.2 b-vetoed Category

The final state of Higgs decaying into tau pair coincide with the one from $Z/\gamma^* \to \tau\tau$ process, this is then an irreducible background for this category. Exploiting the different kinematics of the Higgs decay with respect to other backgrounds is possible to disentangle between them. In the Higgs decaying into $\tau^+\tau^- \to e\ \mu + 4\nu$ the taus are highly boosted and this feature is transferred to the final state leptons, their kinematics then result to be significantly different with respect to process like diboson or $t\bar{t}$. A first difference is that e and μ from the Higgs decay will be more likely "back-to-back", as it is shown in Figure 3.4(a) where the angle between the leptons in the transverse plane $\Delta\phi_{e,\mu} = |\phi_e - \phi_\mu|$ is reported. Furthermore the neutrinos will be more likely collinear with the charged leptons: this feature can be

Category	Selection
b-vetoed	Exactly zero b-tagged taggable jets
	$\Delta\phi(e - \mu) > 1.6$
	$\sum \cos \Delta\phi > -0.4$
b-tagged	Exactly one b-tagged taggable jet
	$\Delta\phi(e - \mu) > 2$
	$\sum \cos \Delta\phi > -0.2$
	$H_T < 100$ GeV
	$P_{T\mu} + P_{Te} + E_T^{miss} < 100$ GeV

Table 3.2: Summary of the dedicated b-tagged and b-vetoed category selections that are employed after the common selections.

matematically seen as the sum of scalar product between missing energy and the leptons four-vectors in the transverse plane, if the vectors are normalised to unit versors then what remains is a relation only between angles:

$$\hat{E}_T^{miss} \cdot (\hat{P}_T^\mu + \hat{P}_T^e) = cos(\Delta\phi_{E_T,\mu}) + cos(\Delta\phi_{E_T,e}) = \sum_\ell cos(\Delta\phi_{E_T,\ell})$$

collinearity implies this sum to be equal to zero as it is shown in Figure 3.4(b). These two feature can be used to distinguish between $e - \mu$ and E_T^{miss} coming from decay of highly boosted and back-to-back object and the one coming from W decays in top or in dibosons backgrounds, in which the leptons are not necessarily back-to-back and the neutrinos not collinear with them. In b-vetoed category these two variables are sufficient to suppress contribution from dibosons, no other selection is applied in this category because it has been shown to not bring significant improvement. The actual selection employed in this category are shown in Table 3.2, while in Table 3.3 the prediction for the number of background and signal events that survises at each selection stage of this category is reported.

3.2.3   b-tagged Category

In the b-tagged category the situation is different, the request of a b-jet enhance backgrounds with b-jet activity as top and single top production. In this category selection on $\Delta\phi(e - \mu)$ and $\sum \cos \Delta\phi$ are employed as described for b-vetoed, since these selections are effective in reducing top and diboson backgrounds. In addition further selection exclusive of this category are employed and are described below.

Given the relatively low jet activity of Higgs events (also in the case of b-associated production), it is possible to separate them from top production which instead is very likely to have two or more highly enegetic jets in the event. Little jet activity is achieved by requesting the sum of the jets P_T in the event to be small, this variable is called H_T and is shown in Figure 3.4(c). The jets used for the calculation of H_T should have $P_T > 30$ GeV, $|\eta| < 4.5$ and JVF > 0.5 (when applicable).

	Common Selections	n(b-jet)=0	$\Delta\phi(e-\mu) > 1.6$	$\sum \cos\Delta\phi > -0.4$
Data	125886	89155	-	- -
Multi-jet	6693 ± 456	6357 ± 461	5322 ± 438	4137 ± 339
$Z \to \ell\ell$	569 ± 48	564 ± 48	516 ± 47	434 ± 44
$W \to \ell\nu$	1625 ± 155	1604 ± 155	1145 ± 125	714 ± 101
Dibosons	9338 ± 48	9235 ± 48	7358 ± 43	4002 ± 31
$t\bar{t}$	40632 ± 106	7707 ± 46	5044 ± 37	3416 ± 31
Single Top	4449 ± 44	1664 ± 27	1124 ± 22	682 ± 18
$Z/\gamma^* \to \tau\tau$	61503 ± 68	60440 ± 67	58078 ± 65	55303 ± 64
Signal			-	-

Table 3.3: Number of data and background events in the b-vetoed channel.

Another feature that distinguish top pair production from Higgs is the higher invariant mass of the former final state (the highest Higgs mass considered for this search is 300 GeV), in the transverse plane all the leptons will tend to have a higher momentum, the sum of electron and muon P_T and E_T^{miss} is then used as a discriminating variable. Figure 3.4(d) shows the distribution of this last analysis variable.

The above described variables defines the b-tagged category, in table 3.2 a summary of all the employed selection variables with their optimized cut values is shown. In Table 3.4 the prediction for the number of background and signal events that survises at each selection stage of this category is reported.

3.2.4 Mass Reconstruction with MMC Technique

Acurate invariant mass reconstuction of a di-τ resonace is a challenging task due to the presence of neutrinos from the τ leptons decay. In case of leptonic decay of both τ leptons a pair of neutrinos for each of them are involved in the final state, the system presents then eight uknowns, which corresponds to the four-momentum of the neutrinos pairs. Four additional kinematic constraint are set by the following equations:

$$\vec{E}_T^{miss} = \vec{P}_T^{mis_1} + \vec{P}_T^{mis_2}$$
$$M_{\tau_i}^2 = m_{mis_i}^2 + m_{vis_i}^2 + 2\mathbf{P}_{vis_i} \cdot \mathbf{P}_{mis_i}$$
(3.1)

where the index i runs over the two τ leptons of the event and assumes the values of 1 or 2. $\vec{P}_T^{mis_i}$, m_{mis_i} and $\mathbf{P}_{mis_i}$ are respectively the transverse momentum, the invariant mass and the four momentum of the pair of neutrinos related to the τ lepton decay i with mass M_τ, the subscript *vis* indicates instead quantities related to the charged lepton from τ lepton decay. The system has still four degrees of freedom, several approximation are possible to further constraint the momentum carried by neutrinos, for example assuming them collinear to the electron or muon from τ lepton decay, however those approximation suffers of mass resolution limitations.

In this analysis, the so-called "Missing Mass Calculator" (MMC) algorithm is used to calculate the most likely di-τ system invariant mass given the event topology, the implementation of the method in this search is based on [129]. The concept of the MMC is to solve equation 3.1 assigning values to the yet undetermined
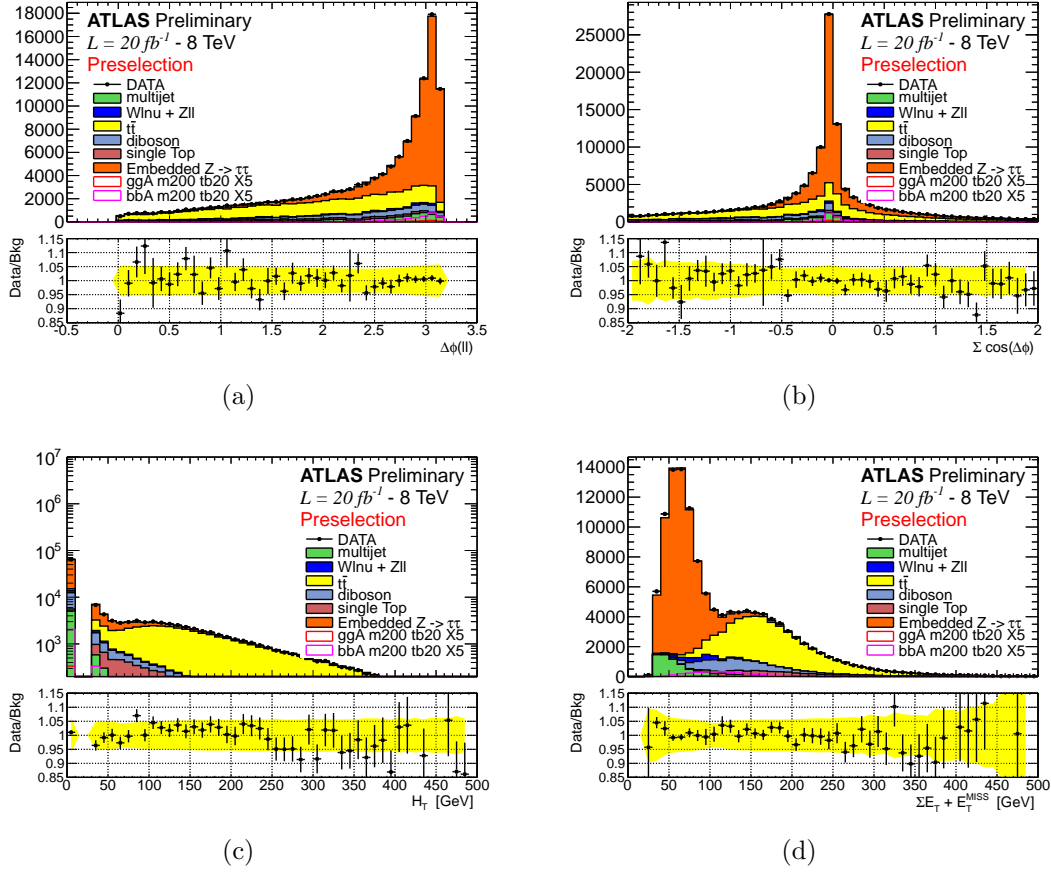
Figure 3.4: Distribution of analysis variable after the selections common to both category, a comparison of the prediction of background model prediction and data is made showing good agreement. The yellow band represents the total systematic uncertainty for the background model prediction.

	n(b-jet)=1	$\Delta\phi$	$\sum \cos \Delta\phi$	$P_{T\mu} + P_{Te} + E_T^{miss}$	H_T
Data	23352	-	-	-	-
Multi-jet 330 $\pm$ 40	208 $\pm$ 27	135 $\pm$ 22	114 $\pm$ 17	100 $\pm$ 15	
$Z \to \ell\ell$	5.2 $\pm$ 1.8	2.3 $\pm$ 1.1	2.3 $\pm$ 1.1	1.7 $\pm$ 1.0	0.9 $\pm$ 0.8
$W \to \ell\nu$	20 $\pm$ 6	15 $\pm$ 6	13 $\pm$ 6	10 $\pm$ 6	10 $\pm$ 6
Dibosons	99 $\pm$ 5	63 $\pm$ 4	36.4 $\pm$ 3.0	14.8 $\pm$ 1.8	13.3 $\pm$ 1.8
$t\bar{t}$	19810 $\pm$ 70	9680 $\pm$ 50	6450 $\pm$ 50	808 $\pm$ 15	350 $\pm$ 10
Single Top	2456 $\pm$ 33	1223 $\pm$ 23	784 $\pm$ 18	122 $\pm$ 7	99 $\pm$ 7
$Z/\gamma^* \to \tau\tau$	952 $\pm$ 9	625 $\pm$ 7	540 $\pm$ 7	482 $\pm$ 6	421 $\pm$ 6
Signal		-	-	-	-

Table 3.4: Number of data and background events in the b-tagged channel.

variables, performing a "scan" over a four dimensional parameter space. The four independent variables are chosen to be $m_{mis_i}^2$ and $cos\theta_i^*$, the latter defined as the angle between the charged lepton from the τ lepton decay and the boost direction of the τ lepton. The di-τ invariant mass of the event can be calculated for each given point of the parameter space that solves equations 3.1, however, the solutions are not all equally likely and the probability of a given τ decay configuration can be predicted by means of simulation (PYTHIA supplemented with TAUOLA package is used). Each point in the parameter space, corresponding to a particular di-τ invariant mass, is then weighted by its probability to occur. The estimator for the final discriminant, the mass of the di-tau system MMC_{mass} , is the maximum of the weighted invariant mass distribution calculated for the scanned points.

The missing energy plays an important role in the MMC method and its resolution has an impact on the calculation of the invariant mass. To improve E_T^{miss} resolution, a scan over a six dimensional parameter space is performed in a similar way as described above, in this case however, $\vec{E}_T^{miss}$ is also considered unknown and a scan is performed on it assigning values according to its uncertainty. The probability of each solution is calculated and the final missing transverse energy is given by the weighted mean of the scanned points.

The final procedure consist in obtaining first an estimate for E_T^{miss} by means of a six dimensional scan over the solution of equations 3.1, successively a four dimensional scan is performed fixing E_T^{miss} to the updated value and calculating the most likely invariant mass of the di-τ system. Figure 3.5 shows the final state invariant mass distribution calculated with MMC_{mass} discriminating variable, the distribution is shown after the common selection and after the full selection of both category.

3.3   Background Modeling and Validation

This section describes the strategies for background modeling and validation. Monte Carlo simulation is extensively used for model either background and signal, the simulations of any process are usually prone to systematics uncertainties due to non-perfect descriptions of pileup effects, underlying event and detector performance, therefore, data-driven background estimation method are employed for the estimate of $Z/\gamma^* \to \tau\tau$ and QCD multi-jet backgrounds, described respectively in
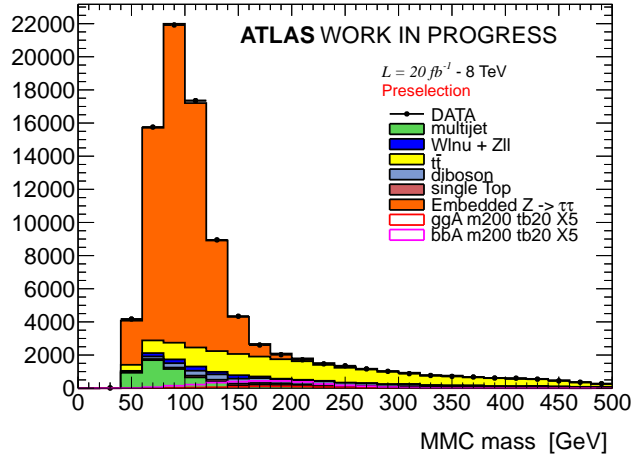
(a)
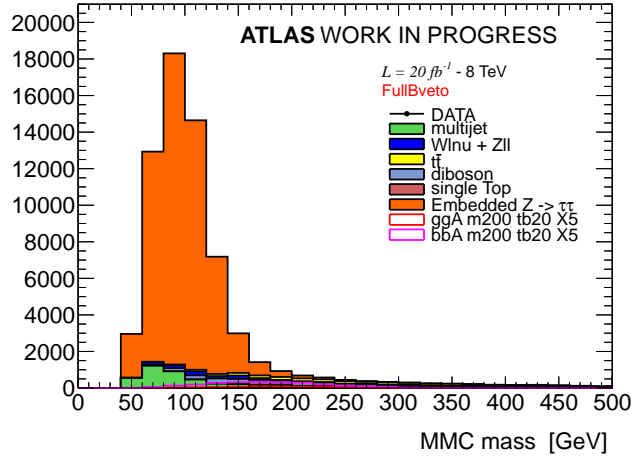
(b)
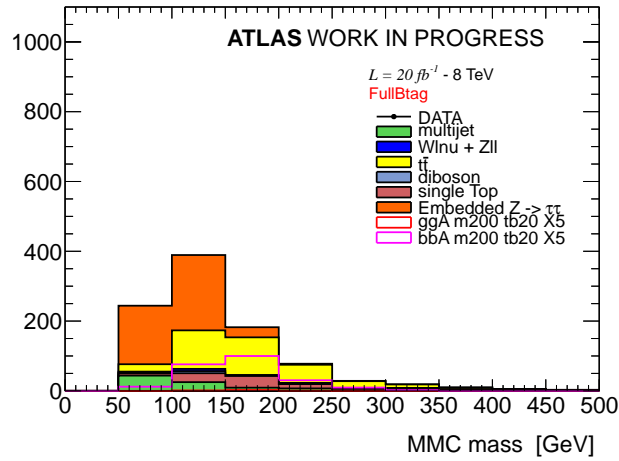
(c)

Figure 3.5: Distribution of the MMC_{mass} for different cuts stage, see text. Left column corresponds to b-tagged category, right column to b-vetoed.

section 3.3.3 and 3.3.2. Other background processes, such as $t\bar{t}$, single top, dibosons, $Z \to ll + \text{jets}$ (where $l = e, \mu$) and W + jets, are estimated using MC predictions. Given the particular importance of $t\bar{t}$ a dedicated study to validate this background has been made and described in section 3.3.1.

A good agreement between data and background model is found after the common selections, this is supported by figure 3.6 which shows few kinematic variables and figure 3.4 which shows analysis selection variables after common selections.

3.3.1 Top Quark Pair Production Validation

The background from top quark pair production is estimated using a sample of simulated events with POWHEG-PYTHIA MC generator. Since this is one of the major backgrounds for this analysis a careful validation is needed, for this purpose a $t\bar{t}$ rich and signal-depleted data control sample is defined using events passing the common selections with the additional requirement of two b-tagged jets. Figures 3.7 and 3.8 show a set of kinematic and analysis selection variables in this data sample, good agreement between data and MC prediction is found: an overall data to background ratio of $0.998 \pm 0.011(\text{stat.}) \pm 0.110(\text{sys.})$ is observed. The total systematic uncertainty on the ratio is dominated by the uncertainty on the b-tagging efficiency.

3.3.2 Multi-jet Background

The QCD multi-jet background represents an important background, especially in the b-veto category, due to its high cross-section and the relatively low cut on lepton P_T used in this analysis. This background is evaluated by a data-driven technique, the so-called ABCD method. The ABCD method consists of splitting the set of data events after the common selections in four samples: the signal sample, defined by the event selections described in Section 3.2 and three signal-depleted control data sample, which do not share events and are designed to be enriched in multi-jets events. The four samples are defined by using the relative sign of the charge of the leptons and isolation selections. To obtain data samples rich in multi-jet background, the selections on both the calorimetric and tracking isolation, described in Section 3.2.1, are inverted with respect to the nominal ones defining anti-isolated leptons. Is then possible to define four data samples: opposite sign (OS) or same sign (SS) with respectively isolated or anti-isolated leptons. Historically the letters A-D are assigned to this data samples for a quicker reference as defined in Table 3.5.

An assumption of the ABCD method is that multi-jet backgrounds populate the OS and SS events independently of lepton isolation criteria, or in other words that the ratio of OS/SS events is uncorrelated with the lepton isolation selections. In this case, the number of QCD events in the signal sample A can be estimated from the yield of multi-jet events in the control samples B, C and D, using the equation

$$N_A = N_B \times \frac{N_C}{N_D} = N_B \times R_{QCD} \tag{3.2}$$

To obtain the multi-jet yields in the data control samples, the contamination from
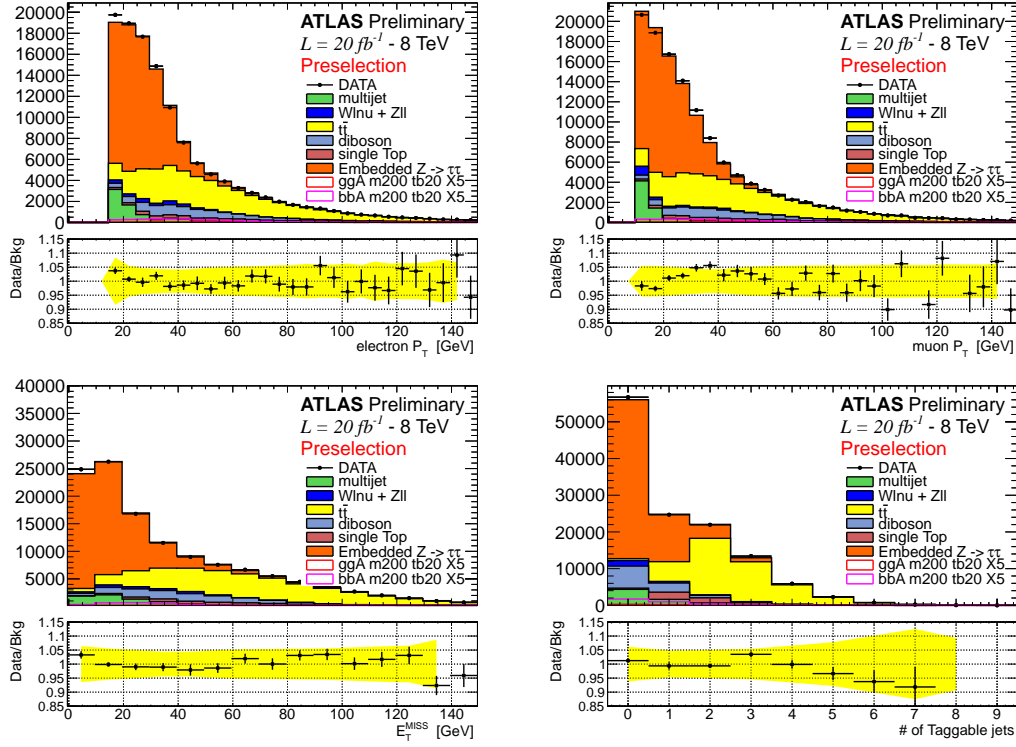
Figure 3.6: Distribution of some kinematic variables after common selections.

sample	Lepton Charge	Lepton Isolation
A (signal sample)	OS	isolated
B	SS	isolated
C	OS	anti-isolated
D	SS	anti-isolated

Table 3.5: QCD background estimation control samples, defined by having leptons with opposite signs (OS) or same signs (SS) and by having the leptons either isolated or anti-isolated.

(a)

(b)

(c)

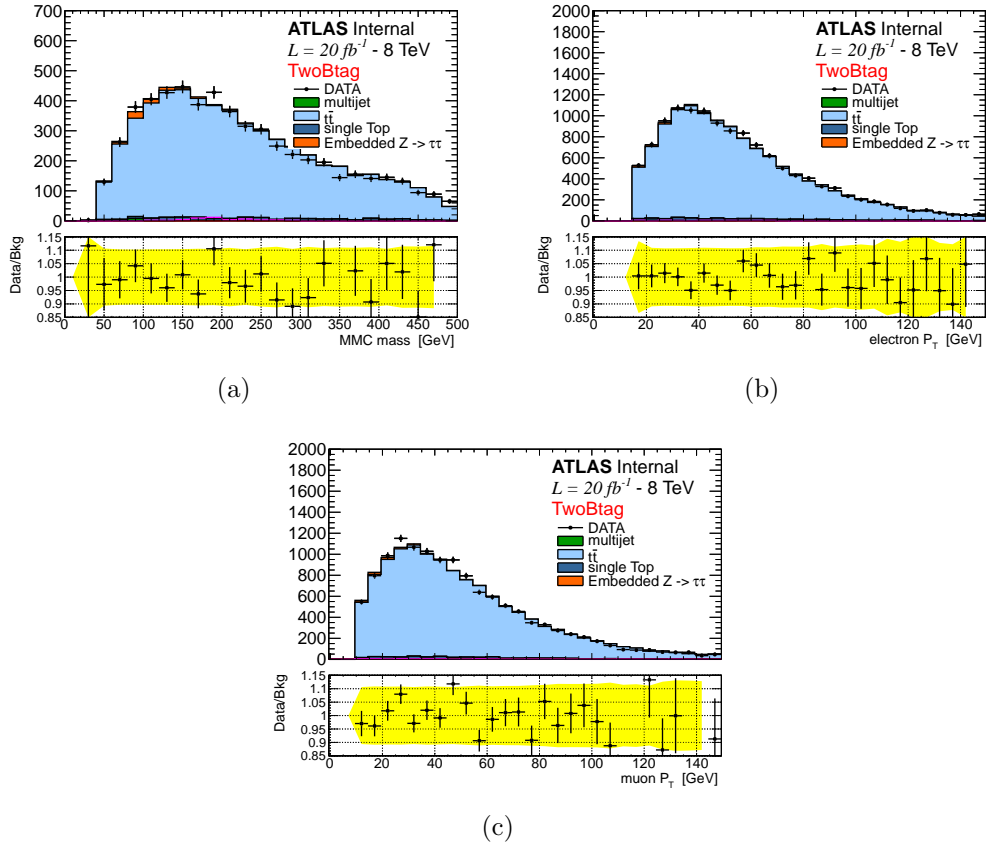Figure 3.7: Distributions of a) the MMC mass, b) the transverse momentum of the electron $P_T(e)$ and c) the transverse momentum of the muon $P_T(\mu)$, for both data and MC in the $t\bar{t}$ control sample. The uncertainties on the points for the ratio plot show the statistical uncertainty on the data to background ratio, whereas the yellow band show the total systematic uncertainty on this ratio.

(a)

(b)

(c)

(d)

Figure 3.8: Distributions of a) $\Delta\phi(e-\mu)$, b) $\sum \cos \Delta\phi$, c) $\sum L_T + E_T^{miss}$ and d) H_T, for both data and MC in the $t\bar{t}$ control sample. The uncertainty on the points for the ratio plot show the statistical uncertainty on the data to background ratio, whereas the yellow band show the total systematic uncertainty on this ratio.
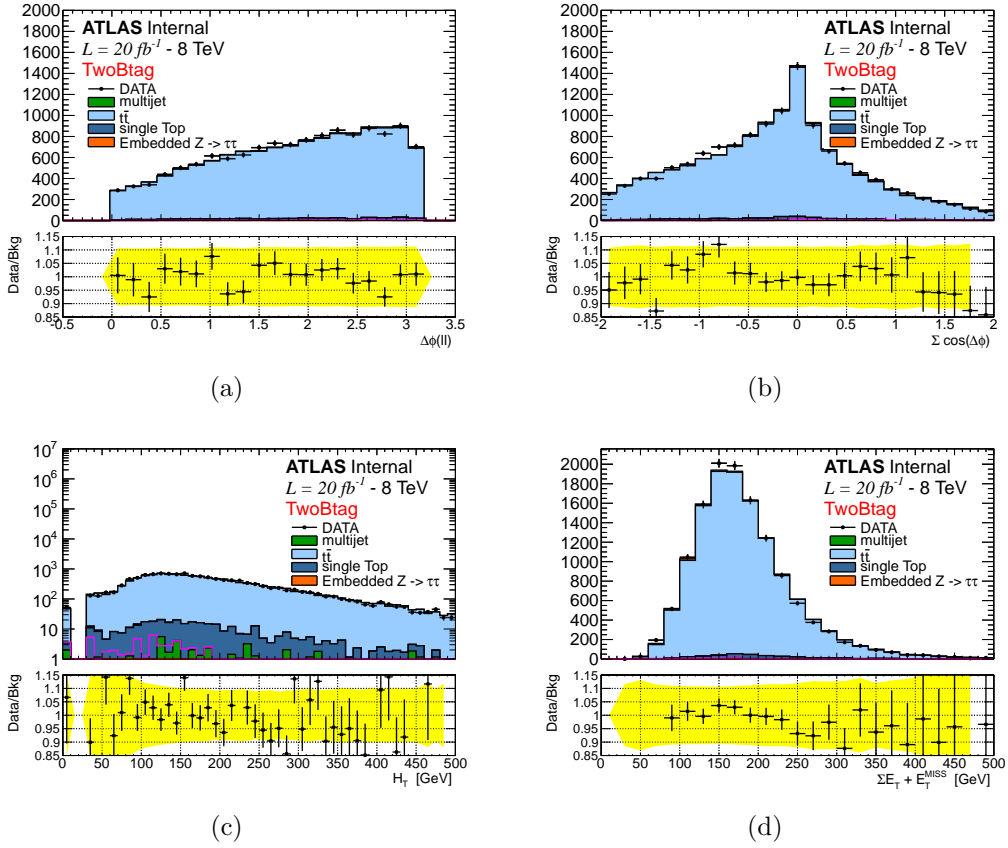
electroweak (W+jets, Z+jets and dibosons) and top processes ($t\bar{t}$ and single top production) are subtracted in each control sample using the MC prediction for their event yield. Tables 3.6 and 3.7 show the event yield for each control sample throughout the full cut-flows along with the predictions of non-QCD multi-jets events which are subtracted. Signal contamination has been checked in all the three control samples for different mass points. For the range of m_A and $\tan\beta$ considered in this analysis, the highest signal contamination is seen in sample B for the mass point $m_A = 300$ GeV and $\tan\beta = 50$, where a contamination of 0.2% is observed[2].

Shapes of kinematic distributions for QCD events are taken from sample B, this sample is expected to have similar kinematic property to the signal sample, however, suffers of either lower statistics and higher contamination with respect to sample C or D. This choice is made to avoid a shape bias due to isolation requirements at trigger level (only the single-electron trigger ask for isolation), figure 3.9 shows the

---

[2] This value is mainly due to b-associated production and, as it scales with the cross section, for $\tan\beta = 20$ would be an order of magnitude smaller.
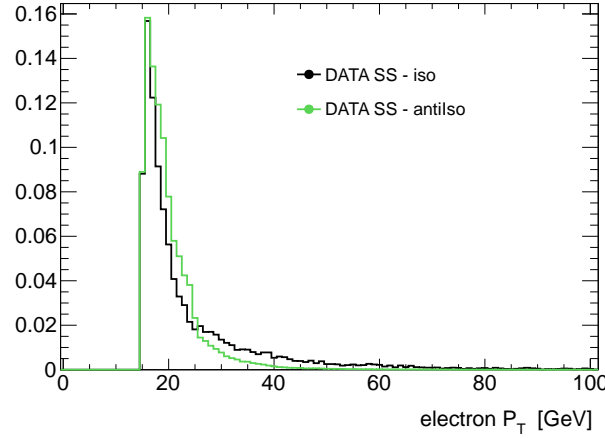
Figure 3.9: Comparison of the electron P_T distribution in sample B and sample D, showing the bias due to the trigger. The histograms are normalized to the same area.

comparison between the electron P_T distributions in sample B and D, in the latter high P_T electrons are suppressed, they do not pass trigger selections. Eventually the trigger isolation requirement could bias also the ratio OS/SS, this possibility has been checked carefully in a dedicated study and reported in Appendix **??**: to a good approximation, such trigger effects cancel out in the ratio OS/SS and no additional systematic is needed.

To test the ABCD method predictions an additional control sample has been defined with the following selections:

- $E_T^{miss} < 20$ GeV

- $H_T < 70$ GeV and $\sum L_T + E_T^{miss} < 50$ GeV

- $0 < MMC_{mass} < 80$ GeV

This control sample is designed to enhance multi-jet background with respect to $Z/\gamma^* \to \tau\tau$ keeping the final state kinematics as similar as possible to the signal sample. Figure 3.10 shows the MMC_{mass} distribution for this control sample with and without b-tagging requirements, agreement between data and the background model is found within statistical and detector related systematics uncertainty.

Systematic uncertainties are assigned on the scaling factor R_{QCD} and on the shape of the discriminating variable MMC_{mass} to take into account any correlation between isolation and charge of the leptons, details on the systematic uncertainty evaluation are addressed in Section **??**.

### 3.3.3 $Z \to \tau\tau$ + Jets Background: Embedding Technique

The background from $Z/\gamma^* \to \tau\tau$ decays is the major background to this analysis, a good understanding of it is then crucial. Unfortunately, for a light Higgs boson, it is impossible to completely separate $Z/\gamma^* \to \tau\tau$ decays from the signal and a

Selection		B	C	D	R_{QCD}
Common Selections	Data	6189	604628	312901	1.929 ± 0.004
	non-QCD	2510 ± 180	1090 ± 30	730 ± 35	
B-tag	Data	419	44619	27257	1.64 ± 0.01
	non-QCD	215 ± 10	310 ± 12	277 ± 13	
$\Delta\phi(e-\mu)$	Data	230	38810	23316	1.67 ± 0.01
	non-QCD	104 ± 6	200 ± 10	175 ± 7	
$\sum \cos \Delta\phi$	Data	149	31379	18779	1.67 ± 0.02
	non-QCD	67 ± 5	127 ± 8	114 ± 6	
$\sum H_T$	Data	83	27781	15626	1.78 ± 0.02
	non-QCD	23 ± 4	25 ± 3	22 ± 3	
$\sum L_T + E_T^{miss}$	Data	71	27735	15590	1.78 ± 0.02
	non-QCD	10 ± 3	22 ± 3	18 ± 2	
$MMC_{mass} > 0.$	Data	70	27634	15522	1.78 ± 0.02
	non-QCD	9 ± 3	20 ± 3	17 ± 2	

Table 3.6: QCD background estimation as a function of the analysis selections for the b-tagged category. The yields for the different control samples, as well as the scaling factor R_{QCD}, are reported. The error on the R_{QCD} is statistical only.

Selection		B	C	D	R_{QCD}
Common Selections	Data	6189	604628	312901	1.929 ± 0.004
	non-QCD	2510 ± 180	1090 ± 30	730 ± 35	
B-veto	Data	5673	558217	284847	1.960 ± 0.004
	non-QCD	2220 ± 180	710 ± 30	415 ± 30	
$\Delta\phi(e-\mu)i$	Data	4610	532583	271404	1.962 ± 0.005
	non-QCD	1700 ± 170	580 ± 30	345 ± 30	
$\sum \cos \Delta\phi$	Data	3417	486747	247712	1.965 ± 0.005
	non-QCD	1120 ± 100	370 ± 20	230 ± 20	
$MMC_{mass} > 0.$	Data	3177	479967	244276	1.965 ± 0.005
	non-QCD	1000 ± 100	300 ± 17	190 ± 20	

Table 3.7: QCD background estimation as a function of the analysis selections for b-veto category. The yields for the different control samples, as well as the scaling factor R_{QCD}, are reported. The error on the R_{QCD} is statistical only.
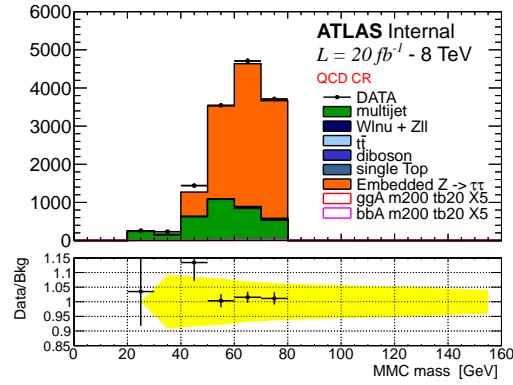
(a)
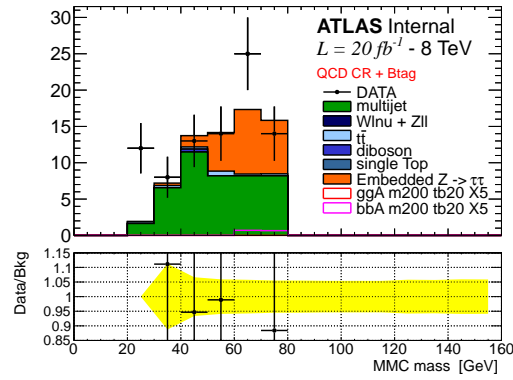
(b)

Figure 3.10: MMC_{mass} distribution for QCD cross check samples defined in section 3.3.2 (a) and for the same control sample when in addition one b-tagged jet is required (b).
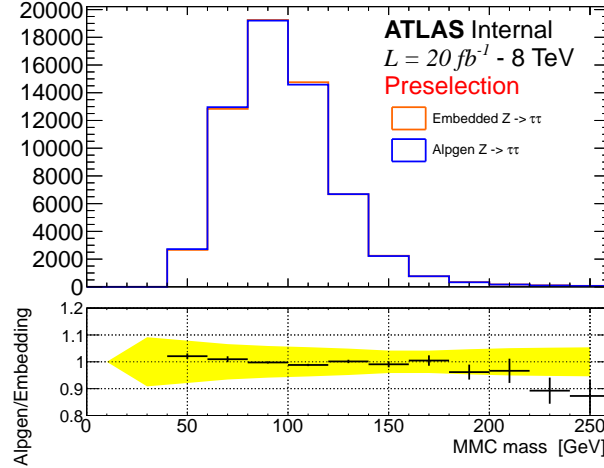
Figure 3.11: Comparison between the embedded $Z/\gamma^* \to \tau\tau$ and ALPGEN for MMC_{mass} distributions.

signal free data control sample cannot be defined. However, thanks to the small Higgs coupling to muons, $Z \to \mu\mu$ decays provide a good starting point to model $Z/\gamma^* \to \tau\tau$ events in a data-driven way. An hybrid Data-MC sample, known as "Embedding" is used to model the $Z/\gamma^* \to \tau\tau$ background: $Z \to \mu\mu$ candidates are selected in data, then, the two muons from the Z decay are substituted with the decay products from simulated taus, this means that the energy deposit and tracks in a cone around the muon are subtracted and substituted with the one from τ decay, those taus have the same kinematics as the original muons. Further details on this technique may be found in [86, 87].

Trigger is not simulated in the Embedding samples, the event yield is normalized to ALPGEN $Z/\gamma^* \to \tau\tau$ at common selection stage. Furthermore a set of corrections, as described in [88], are applied to unfold from the original $Z \to \mu\mu$ trigger and reconstruction efficiency, then trigger and reconstruction efficiency for a $e - \mu$ final state are emulated by means of event weight.

The Embedding technique has been validated in several studies, detailed in [86, 88], which show a good description of data and $Z/\gamma^* \to \tau\tau$ MC by Embedding. In the context of this analysis, figures 3.11 and 3.12 show comparisons of various kinematic variables between data, Embedding and ALPGEN $Z/\gamma^* \to \tau\tau$ simulated events at common selection. No significant deviation is seen between the MMC_{mass} distribution of the Embedding and ALPGEN samples, however other relevant variables for this analysis, such as the E_T^{miss} and the number of b-jets, are slightly better described by Embedding.

The Embedding sample is based on selecting $Z \to \mu\mu$ candidates in data, the selections assure a rather pure $Z \to \mu\mu$ sample, however further selections used in this analysis, for example the b-tagging requirements, could enhance the contamination fraction from other processes. Dedicated studies have been made to estimate the $t\bar{t}$ and QCD multi-jet contamination in the Embedding sample. The $t\bar{t}$ contamination is estimated by evaluating the Embedding yield in a two b-tag control sample (as
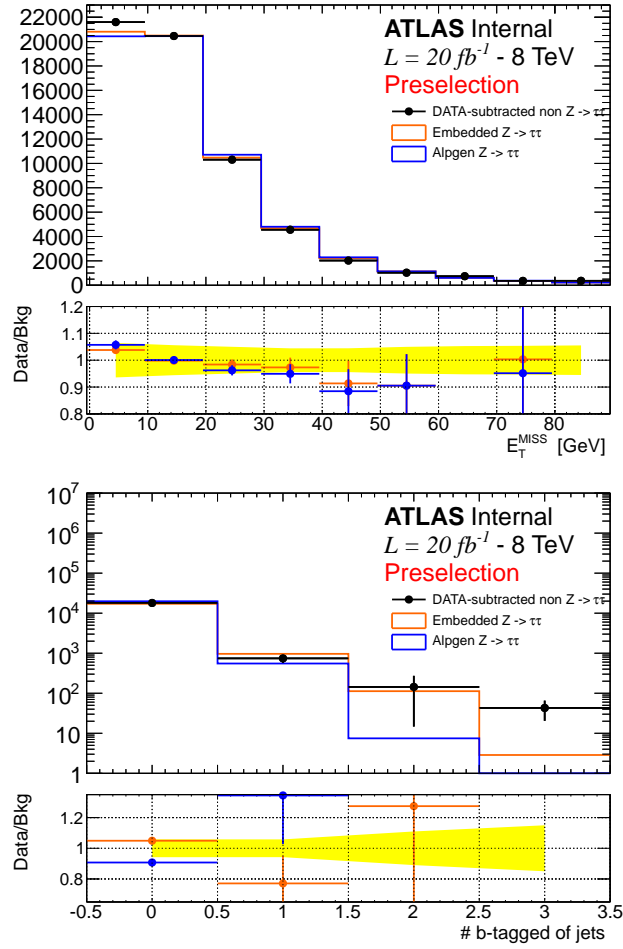
Figure 3.12: Comparison between embedded $Z/\gamma^* \to \tau\tau$ and ALPGEN for E_T^{miss} and the number of b-tagged jets distributions. Data are superimposed, with the contribution of non-$Z/\gamma^* \to \tau\tau$ are subtracted.

	Embedding yield in control sample	Transfer factor	Estimated events in signal sample	Contamination
b-tag	84 ± 9	$(2.6 \pm 0.1) \times 10^{-2}$	2.2 ± 0.2	0.5 %
b-veto	84 ± 9	$(1.74 \pm 0.02) \times 10^{-1}$	15 ± 2	0.03 %

Table 3.8: Evaluating Embedding $t\bar{t}$ contamination using a two b-tag CR. The transfer factor is the multiplicative factor that allows to estimate events in signal sample from the control sample.

	Embedding yield in control sample	Transfer factor	Estimated events in signal sample	Contamination
B-tag	12 ± 3	$(7 \pm 1) \times 10^{-3}$	$(8.4 \pm 0.3) \times 10^{-2}$	0.03 %
B-veto	390 ± 20	$(2.5 \pm 0.1) \times 10^{-2}$	10.0 ± 0.5	0.02 %

Table 3.9: Evaluating Embedding contamination due to QCD multi-jet using ABCD method, the control sample here is with OS anti-isolated events (sample C). The transfer factor is the multiplicative factor that allows to estimate events in signal sample from the control sample, in this case is N_B/N_D and is evaluated using mu-mu final state with the same kinematic selection used in the definition of the Embedding sample.

described in Section 3.3.1), these events are assumed to be solely from $t\bar{t}$ and their yield in the signal sample is extrapolated using MC simulation. Table 3.8 shows a summary for the top contamination in Embedding. The multi-jet contamination can be estimated starting from the Embedding yield in (ABCD) sample C, assuming all events in this control sample as QCD multi-jet events, the contamination in the signal sample can be estimated by means of the ABCD method (see Section 3.3.2). The R_{QCD} factor, in this case, is evaluated using a $\mu - \mu$ final state with same kinematic selections as for Embedding $Z \rightarrow \mu\mu$ candidate. Table 3.9 shows the estimated contamination of QCD multi-jet in Embedding. Contamination effects are considered negligible.

Bibliography

[1] G. Altarelli, *"Collider Physics within the Standard Model: a Primer,"* arXiv:1303.2842 .

[2] S. P. Martin, *"A Supersymmetry primer,"* In *Kane, G.L. (ed.): Perspectives on supersymmetry II* 1-153 [hep-ph/9709356].

[3] A. Djouadi, *The Anatomy of Electroweak Symmetry Breaking Tome II: The Higgs Bosons in the Minimal Supersymmetric Model*, Phys. Rep. 459 (2008) 1.

[4] S. Heinemeyer *et al.* [LHC Higgs Cross Section Working Group Collaboration], "Handbook of LHC Higgs Cross Sections: 3. Higgs Properties," arXiv:1307.1347

[5] S. Dittmaier *et al.* [LHC Higgs Cross Section Working Group Collaboration], *"Handbook of LHC Higgs Cross Sections: 1. Inclusive Observables,"* arXiv:1101.0593

[6] Michael E. Peskin, Dan V. Schroeder, *An Introduction To Quantum Field Theory*, Westview Press, 1995.

[7] S. L. Glashow, Partial Symmetries of Weak Interactions, Nuc. Phys. 22 (1961) 579.

[8] A. Salam, Weak and Electromagnetic Interactions, Conf. Proc. C 680519 (1968) 367. Originally printed in Svartholm: Elementary Particle Theory, proceedings of the Nobel Symposium held 1968 at Lerum, Sweden.

[9] S. Weinberg, A Model of Leptons, Phys. Rev. Lett. 19 (1967) 1264.

[10] H. Fritsch, M. Gell-Mann, and H. Leutwyler, Advantages of the Color Octet Gluon Picture, Phys. Lett. B 47 (1973) 365.

[11] F. Englert and R. Brout, *Broken Symmetry and the Mass of Gauge Vector Mesons*, Phys. Rev. Lett. **13** (1964) 321.

[12] P. W. Higgs, *Broken symmetries, massless particles and gauge fields*, Phys. Lett. **12** (1964) 132.

[13] P. W. Higgs, *Broken Symmetries and the Masses of Gauge Bosons*, Phys. Rev. Lett. **13** (1964) 508.

[14] P. W. Higgs, *Spontaneous Symmetry Breakdown without Massless Bosons*, Phys. Rev. **145** (1966) 1156.

[15] T. W. B. Kibble, Symmetry Breaking in NonAbelian Gauge Theories, Phys. Rev. 155 (1967) 1554.

[16] The ATLAS Collaboration, *Observation of a new particle in the search for the Standard Model Higgs boson with the ATLAS detector at the LHC*, Physics Letters B **716** (2012) 1–29.

[17] The CMS Collatoration, *Observation of a new boson at a mass of 125 GeV with the CMS experiment at the LHC*, Physics Letters B **716** (2012) 30–61.

[18] W. Hollik, *"Electroweak theory,"* hep-ph/9602380.

[19] The Review of Particle Physics, J. Beringer et al. (Particle Data Group), Phys. Rev. D86, 010001 (2012) and 2013 partial update for the 2014 edition.

[20] The ALEPH, CDF, D0, DELPHI, L3, OPAL and SLD Collaborations, the LEP Electroweak Working Group, Tevatron Working Group and SLD Electroweak and Heavy Flavour Working Groups, *Precision Electroweak Measurements and Constraints on the Standard Model*, arXiv:1012.2367. Updated for 2012 winter conferences, March 2012.

[21] The Gfitter Group, M. Baak, et al., Updated Status of the Global Electroweak Fit And constraints on New Physics, Eur. Phys. J. C 72 (2012) 2003. Updated for 2012 winter conferences, March 2012, http://gfitter.desy.de.

[22] G.W. Bennett et al., Phys. Rev. Lett. 89, 101804 (2002); Erratum ibid. Phys. Rev. Lett. 89, 129903 (2002); G.W. Bennett et al., Phys. Rev. Lett. 92, 161802 (2004); G.W. Bennett et al., Phys. Rev. D73, 072003 (2006).

[23] B. Bhattacherjee, S. S. Biswal and D. Ghosh, *Top quark forward-backward asymmetry at Tevatron and its implications at the LHC*, Phys. Rev. D **83** (2011) 091501 [arXiv:1102.0545 [hep-ph]].

[24] M. Veltman, Acta. Phys. Pol. B8 (1977) 475.

[25] S. Weinberg, Gauge Hierarchies, Phys. Lett. B 82 (1979) 387.

[26] M. Veltman, The InfraredUltraviolet Connection, Acta Phys. Polon. B 12 (1981) 437.

[27] C. Smith and G. Ross, The Real Gauge Hierarchy Problem, Phys. Lett. B 105 (1981) 38.

[28] F. Zwicky, Spectral Displacement of Extra Galactic Nebulae, Helv. Phys. Acta 6 (1933) 110.

[29] E. W. Kolb and M. S. Turner, The Early Universe, Front. Phys. 69 (1990) 1.

[30] The WMAP Collaboration, D. N. Spergel et al., First Year Wilkinson Microwave Anisotropy Probe (wmap) Observations: Determination of Cosmological Parameters, Astrophys. J. Suppl. 148 (2003) 175.

[31] H. M. Georgi and S. L. Glashow, Unity of All ElementaryParticle Forces, Phys. Rev. Lett. 32 (1974) 438.

[32] J. C. Pati and A. Salam, Lepton Number as the Fourth Color, Phys. Rev. D 10 (1974) 275.

[33] P. Fayet, Phys. Lett. B 64, 159 (1976).

[34] P. Fayet, Phys. Lett. B 69, 489 (1977), Phys. Lett. B 84, 416 (1979).

[35] G.R. Farrar and P. Fayet, Phys. Lett. B 76, 575 (1978).

[36] S. Martin, in Perspectives on Supersymmetry, Ed. G.L. Kane, World Scientific, Singa- pore, 1998, hep-ph/9709356.

[37] For reviews on the MSSM, see: P. Fayet and S. Ferrara, Phys. Rep. 32 (1977) 249; H.P. Nilles, Phys. Rep. 110 (1984) 1; R. Barbieri, Riv. Nuovo Cim. 11N4 (1988) 1; R. Arnowitt and Pran Nath, Report CTP-TAMU-52-93; J. Bagger, Lectures at TASI-95, hep-ph/9604232.

[38] H. E. Haber and G. Kane, Phys. Rep. 117 (1985) 75.

[39] M. Drees and S. Martin, CLTP Report (1995) and hep-ph/9504324.

[40] D.J.H. Chung, L.L. Everett, G.L. Kane, S.F. King, J. Lykken and L.T. Wang, Phys. Rept. 407 (2005) 1.

[41] M. Drees, R.M. Godbole and P. Roy, Theory and Phenomenology of Sparticles, World Scientific, Spring 2004.

[42] L. Girardello and M.T. Grisaru, Nucl. Phys. B194 (1982) 65.

[43] Y. Okada, M. Yamaguchi and T. Yanagida, Prog. Theor. Phys. 85 (1991) 1; ibid. Phys. Lett. B262 (1991) 54; J.R. Ellis, G. Ridolfi and F. Zwirner, Phys. Lett. B257 (1991) 83; ibid. Phys. Lett. B262 (1991) 477; H.E. Haber and R. Hempfling, Phys. Rev. Lett. 66 (1991) 1815.

[44] A. Djouadi and S. RosiersLees (conv.) et al., Summary Report of the MSSM Working Group for the GDRSupersym trie, hep-ph/9901246.

[45] K. Inoue, A. Komatsu and S. Takeshita, Prog. Theor. Phys 68 (1982) 927; (E) ibid. 70 (1983) 330.

[46] E. Witten, Nucl. Phys. B188 (1981) 513; ibid Nucl. Phys. B202 (1982) 253; N. Sakai, Z. Phys. C11 (1981) 153; S. Dimopoulos and H. Georgi, Nucl. Phys. B193 (1981) 150; R.K. Kaul and P. Majumdar, Nucl. Phys. B199 (1982) 36.

[47] J.F. Donoghue and L.F. Li, Phys. Rev. 19 (1979) 945.

[48] J.F. Gunion and H.E. Haber, Nucl. Phys. B278 (1986) 449.

[49] J.F. Gunion and H.E. Haber, Nucl. Phys. B272 (1986) 1; (E) hep-ph/9301205.

[50] M. Frank et al., The Higgs Boson Masses and Mixings of the Complex MSSM in the FeynmanDiagrammatic Approach, JHEP 0702 (2007) 47.

[51] M. Carena, S. Heinemeyer, C. E. M. Wagner, and G. Weiglein, *Suggestions for benchmark scenarios for MSSM Higgs boson searches at hadron colliders*, Eur. Phys. J. **C26** (2003) 601–607, `hep-ph/0202167`.

[52] S. Heinemeyer, O. Stal, and G. Weiglein, *Interpreting the LHC Higgs Search Results in the MSSM*, Phys. Lett. B 710 (2012) 201206, arXiv:1112.3026.

[53] The ATLAS Collaboration , *Constraints on New Phenomena via Higgs Boson Coupling Measurements with the ATLAS Detector.* ATLAS-CONF-2014-010.

[54] L. Maiani, A. Polosa, and V. Riquer, Bounds to the Higgs Sector Masses in Minimal Supersymmetry from LHC Data, arXiv:1305.2172.

[55] A. Djouadi, L. Maiani, G. Moreau, A. Polosa, J. Quevillon, et al., The post-Higgs MSSM scenario: Habemus MSSM?, arXiv:1307.5205.

[56] L. Evans and P. Bryant, *LHC Machine*, JINST **3** (2008) S08001.

[57] The ATLAS Collaboration, G. Aad et al., *The ATLAS Experiment at the CERN Large Hadron Collider*, JINST **3** (2008) S08003.

[58] J. Haffner, *The CERN accelerator complex*, OPEN-PHO-ACCEL-2013-056.

[59] CMS Collaboration, CMS technical proposal, CERN-LHCC-94-38.

[60] LHCb Collaboration, LHCb technical proposal, CERN-LHCC-98-004.

[61] ALICE Collaboration, ALICE: Technical proposal for a large ion collider experiment at the CERN LHC, CERN-LHCC-95-71, CERN, 1995,

[62] G. S. Guralnik, C.R. Hagen and T. W. B. Kibble Phys.Rev.Lett. **13** (1964) 585.

[63] The ATLAS Collaboration, *Luminosity Determination in pp Collisions at $\sqrt{s} = 7$ TeV using the ATLAS Detector in 2011*, ATLAS-CONF-2011-116.

[64] ALEPH, DELPHI, L3 and OPAL Collaboration, *Search for neutral MSSM Higgs bosons at LEP*, Eur. Phys. J. **C47** (2006) 547.

[65] *Combined CDF and D0 upper limits on MSSM Higgs boson production in tau-tau final states with up to 2.2 fb^{-1} of data*, `arXiv:1003.3363 [hep-ex]`.

[66] The CMS Collaboration, S. Chatrchyan et al., `arXiv:1104.1619 [hep-ex]` `[hep-ex]`.

[67] The ATLAS Collaboration , *Search for the neutral Higgs bosons of the Minimal Supersymmetric Standard Model in pp collisions at $\sqrt{s} = 7$ TeV with the ATLAS detector*, `arXiv:1211.6956 [hep-ex]`.

[68] S. Heinemeyer, O. Stål and G. Weiglein, *Interpreting the LHC Higgs search results in the MSSM*, Phys.Lett. **B710** (2012) 201–206, `arXiv:1112.3026 [hep-ph]`.

[69] A. Arbey, M. Battaglia, A. Djouadi and F. Mahmoudi, *The Higgs sector of the phenomenological MSSM in the light of the Higgs boson discovery*, JHEP **1209** (2012) 107, `arXiv:1207.1348 [hep-ph]`.

[70] M. L. Mangano et al., *ALPGEN, a generator for hard multiparton processes in hadronic collisions*, JHEP **07** (2003) 001.

[71] J. Alwall et al., *Comparative study of various algorithms for the merging of parton showers and matrix elements in hadronic collisions*, Eur. Phys. J. **C53** (2008) 473, `arXiv:0706.2569`.

[72] S. Frixione and B. R. Webber, *Matching NLO QCD computations and parton shower simulations*, JHEP **06** (2002) 029, `hep-ph/0204244`.

[73] B. P. Kersevan and E. Richter-Was, *The Monte Carlo Event Generator AcerMC 2.0 with Interfaces to PYTHIA 6.2 and HERWIG 6.5*, `arXiv:0405247v1 [hep-ph]`.

[74] G. Corcella et al., *HERWIG 6: an event generator for hadron emission reactions with interfering gluons (including supersymmetric processes)*, JHEP **01** (2001) 010.

[75] J. M. Butterworth, J. R. Forshaw, and M. H. Seymour, *Multiparton Interactions in Photoproduction at HERA*, Z. Phys. **C72** (1996) 637.

[76] T. Binoth, M. Ciccolini, N. Kauer, and M. Kramer, *Gluon-induced W-boson pair production at the LHC*, JHEP **12** (2006) 046.

[77] A. S. et al., *Higgs boson production in gluon fusion*, JHEP **02** (2009) 029.

[78] T. Gleisberg et al., *Event generation with SHERPA 1.1*, JHEP **02** (2009) 007.

[79] J. Pumplin, D. R. Stump, J. Huston, H. L. Lai, P. M. Nadolsky and W. K. Tung, "New generation of parton distributions with uncertainties from global QCD analysis," JHEP **0207** (2002) 012 [hep-ph/0201195].

[80] H. -L. Lai, M. Guzzi, J. Huston, Z. Li, P. M. Nadolsky, J. Pumplin and C. -P. Yuan, "New parton distributions for collider physics," Phys. Rev. D **82** (2010) 074024 [arXiv:1007.2241 [hep-ph]].

[81] The ATLAS Collaboration, *ATLAS Monte Carlo Tunes for MC09*, ATL-PHYS-PUB-2010-002.

[82] S. Jadach, J. H. Kuhn and Z. Was, *TAUOLA - a library of Monte Carlo programs to simulate decays of polarized τ leptons*, Comput. Phys. Commun. **64** (1990) 275.

[83] E. Barberio, B. V. Eijk and Z. Was, *Photos - a universal Monte Carlo for QED radiative corrections in decays*, Comput. Phys. Commun. **66** (1991) 115.

[84] The GEANT4 Collaboration, S. Agostinelli et al., *GEANT4 - a simulation toolkit*, Nucl. Instrum. Meth. **A506** (2003) 250.

[85] The ATLAS Collaboration, G. Aad et al., *The ATLAS Simulation Infrastructure*, ATLAS-SOFT-2010-01-004, submitted to Eur. Phys. J. C., `arXiv:1005.4568`.

[86] The ATLAS Collaboration, *Estimation of $Z/\gamma^* \to \tau\tau$ Background in VBF $H \to \tau\tau$ Searches from $Z \to \mu\mu$ Data using an Embedding Technique*, ATL-PHYS-INT-2009-109.

[87] The ATLAS Collaboration, *Search for the Standard Model Higgs boson in the $H \to \tau\tau$ decay mode with 4.7 f b1 of ATLAS detactor*, Tech. Rep. ATLAS-CONF-2012-014, CERN, Geneva, Mar, 2012.

[88] The ATLAS Collaboration, *Search for the Standard Model Higgs boson $H \to \tau\tau$ decays with the ATLAS detector*, ATL-COM-PHYS-2013-722.

[89] T. S. et al., Z *physics at LEP 1*, CERN 89-08 **3** (1989) 143.

[90] The ATLAS Collaboration, Inner Detector: Technical Design Report, CERN/LHCC/97-016/017 (1997).

[91] The ATLAS Collaboration, G. Aad et al., The ATLAS Experiment at the CERN Large Hardon Collider, 2008 JINST 3 S08003.

[92] A. Bazan, T. Bouedo, P. Ghez, M. Marino and C. Tull, "The Athena data dictionary and description language," eConf C **0303241** (2003) MOJT010 [cs/0305049 [cs-se]].

[93] The ATLAS Collaboration, *Expected Performance of the ATLAS Experiment - Detector, Trigger and Physics*, CERN-OPEN-2008-020, `arXiv:0901.0512`.

[94] T. Cornelissen et al., Concepts, Design and Implementation of the ATLAS New Tracking, ATLAS Note ATL-SOFT-PUB-2007-007 (2007).

[95] Kalman, R. E. (1960). *"A New Approach to Linear Filtering and Prediction Problems"*. Journal of Basic Engineering 82 (1): 3545. doi:10.1115/1.3662552

[96] The ATLAS Collaboration, Performance of primary vertex reconstruction in proton-proton collisions at $s = sqrt(7)$ TeV in the ATLAS experiment. ATLAS-CONF-2010-069.

[97] R. Fruhwirth, W. Waltenberger, P. Vanlaer, *Adaptive vertex fitting*, J. Phys. G34 (2007).

[98] The ATLAS Collaboration, *Characterization of Interaction-Point Beam Parameters Using the pp Event-Vertex Distribution Reconstructed in the ATLAS Detector at the LHC*, ATL-CONF-2010-027.

[99] The ATLAS collaboration, *Expected electron performance in the ATLAS experiment*, ATL-PHYS-PUB-2011-006

[100] The ATLAS Collaboration, *Electron reconstruction and identification efficiency measurements with the ATLAS detector using the 2011 LHC proton-proton collision data*, CERN-PH-EP-2014-040, arXiv:1404.2240

[101] The ATLAS Collaboration, G. Aad et al., *Electron performance measurements with the ATLAS detector using the 2010 LHC proton-proton collision data*, Eur.Phys.J. C72 (2012) 1909.

[102] S. Hassini, et al., *A muon identification and combined reconstruction procedure for the ATLAS detector at the LHC using the (MUONBOY, STACO, MuTag) reconstruction packages*, NIM A572 (2007) 7779.

[103] The ATLAS Collaboration, G. Aad et al., *Preliminary results on the muon reconstruction efficiency, momentum resolution, and momentum scale in ATLAS 2012 pp collision data*, ATLAS-CONF-2013-088, CERN, 2013,

[104] M. Cacciari, G. P. Salam, and G. Soyez, *FastJet user manual*, Eur.Phys.J. C72 (2012) 1896.

[105] W. Lampl et al., *Calorimeter Clustering Algorithms : Description and Performance*, ATL-LARG-PUB-2008-002.

[106] M. Cacciari, G. P. Salam, and G. Soyez, *The anti-kt jet clustering algorithm*, JHEP 04 (2008) 63.

[107] E. Abat, J. Abdallah, T. Addy, P. Adragna, et al., *Combined performance studies for electrons at the 2004 ATLAS combined test-beam*, JINST 5 (2010) P11006.

[108] ATLAS Collaboration, *Jet energy measurement with the ATLAS detector in proton-proton collisions at $\sqrt{s} = 7$ TeV*, Submitted to EPJ (2011) , arXiv:1112.6426

[109] The ATLAS Collaboration, *Pile-up corrections for jets from proton-proton collisions at ATLAS in 2011*, ATLAS-CONF-2012-064, July, 2012.

[110] M. Cacciari and G. P. Salam, *Pileup subtraction using jet areas*, Phys.Lett. B659 (2008) 119.

[111] The ATLAS Collaboration, G. Aad et al., *Jet energy resolution in proton-proton collisions at $\sqrt{s} = 7$ TeV recorded in 2010 with the ATLAS detector*, Eur.Phys.J. C73 (2013) 2306

[112] The ATLAS collaboration, *Jet energy scale and its systematic uncertainty in proton-proton collisions at $\sqrt{s} = 7$ TeV with ATLAS 2011 data*, ATLAS-CONF-2013-004

[113] The ATLAS Collaboration, *Data-Quality Requirements and Event Cleaning for Jets and Missing Transverse Energy Reconstruction with the ATLAS Detector in Proton-Proton Collisions at a Center-of-Mass Energy of $\sqrt{s} = 7$ TeV*, ATLAS-CONF-2010-038.

[114] G. Piacquadio, C. Weiser, *A new inclusive secondary vertex algorithm for b-jet tagging in ATLAS*, JPCS 119 (2008) 032032

[115] The ATLAS Collaboration, G. Aad et al., *Commissioning of the ATLAS high-performance b-tagging algorithms in the 7 TeV collision data, ATLAS-CONF-2011-102*, CERN, 2011, ATLAS-CONF-2011-102.

[116] The ATLAS Collaboration, *Measuring the b-tag efficiency in a ttbar sample with 4.7 fb^{-1} of data from the ATLAS detector* ATLAS-CONF-2012-097.

[117] The ATLAS Collaboration, *Calibration of b-tagging using dileptonic top pair events in a combinatorial likelihood approach with the ATLAS experiment* ATLAS-CONF-2014-004.

[118] The ATLAS Collaboration, *Reconstruction and Calibration of Missing Transverse Energy and Performance in Z and W events in ATLAS Proton-Proton Collisions at $\sqrt{s}$=7 TeV*, ATLAS-CONF-2011-080.

[119] ATLAS Collaboration, G. Aad et al., Performance of missing transverse momentum reconstruction in proton-proton collisions at 7 TeV with ATLAS, Eur.Phys.J. C72 (2012) 1844.

[120] TheATLAS Collaboration, *Performance of the Reconstruction and Identification of Hadronic tau Decays in ATLAS with 2011 Data*, ATLAS-CONF-2012-142.

[121] The ATLAS Collaboration, G. Aad et al., *Performance of the ATLAS trigger system in 2010*, Eur.Phys.J. C72 (2012) 1849.

[122] The ATLAS Collaboration, G. Aad et al., *Performance of the ATLAS muon trigger in 2011*, ATLAS-CONF-2012-099, CERN, 2012.

[123] The ATLAS Collaboration, G. Aad et al., *Performance of the ATLAS electron and photon trigger in p-p collisions at $\sqrt{s} = 7$ TeV in 2011*, ATLAS-CONF-2012-048, CERN, 2012.

[124] M. Dobbs and J.B. Hansen, *The HepMC C++ Monte Carlo Event Record for High Energy Physics*, Computer Physics Communications, ATL-SOFT-2000-001.

[125] The ATLAS Collaboration, *Evidence for the spin-0 nature of the Higgs boson using ATLAS data* , Phys. Lett. B 726 (2013), pp. 120-144.

[126] The ATLAS Collaboration, *Measurements of Higgs boson production and couplings in diboson final states with the ATLAS detector at the LHC*, Phys. Lett. B 726 (2013), pp. 88-119.

[127] The CMS Collaboration, *"Evidence for the direct decay of the 125 GeV Higgs boson to fermions,"* arXiv:1401.6527 [hep-ex].

[128] The CMS Collaboration, *Higgs boson width from on- vs. off-shell production and decay to Z-boson pairs* , arXiv:1405.3455.

[129] A. Elagin, P. Murat, A. Pranko, and A. Safonov, *A New Mass Reconstruction Technique for Resonances Decaying to di-tau*, `arXiv:1012.4686 [hep-ex]`. * Temporary entry *.

[130] T. A. Collaboration, *Search for neutral MSSM Higgs bosons decaying to $\tau\tau$ pairs in proton-proton collisions at with the ATLAS detector*, Physics Letters B **705** (2011) no. 3, 174 – 192.

[131] The ATLAS Collaboration, *Data-driven estimation of the background to charged Higgs boson searches using hadronically-decaying tau final states in AT-LAS,* ATLAS-CONF-2011-051.

[132] The ATLAS Collaboration, *Measurement of the $Z \to \tau\tau$ cross section with the ATLAS detector*, Phys. Rev. D **84** (2011) 112006.

[133] T. A. Collaboration, *Search for the neutral Higgs bosons of the Minimal Supersymmetric Standard Model in pp collisions at $\sqrt{s} = 7$ TeV with the ATLAS detector*, JHEP , `arXiv:1211.6956`.

[134] Atlas statistics forum, *ABCD method in searches*, link

[135] The ATLAS Collaboration, *Search for Neutral MSSM Higgs Bosons H to $\tau\tau$ to $l\tau_h$ with the ATLAS Detector in 7 TeV Collisions*, ATL-COM-PHYS-2012-094.

[136] The ATLAS Collaboration, *Search for neutral Higgs Bosons in the decay mode $H \to \tau\tau \to ll+4\nu$ in proton proton collision at $\sqrt{7}$ TeV with the ATLAS Detector*, ATL-COM-PHYS-2011-758.

[137] The Atlas Collaboration, *Measurement of the ttbar production cross-section in pp collisions at $\sqrt{s} = 8$ TeV using e-mu events with b-tagged jets* . ATLAS-CONF-2013-097.

[138] T. Sjostrand, S. Mrenna and P. Skands, *PYTHIA 6.4 physics and manual*, JHEP **05** (2006) 026.

[139] A. B. et al., *Rivet user manual*, `arXiv:1003.0694 [hep-ph]`.

[140] The ATLAS and CMS Collaborations, *Procedure for the LHC Higgs boson search combination in summer 2011*, ATL-PHYS-PUB-2011-011, ATL-COM-PHYS-2011-818, CMS-NOTE-2011-005.

[141] W. Verkerke and D. P. Kirkby, *The Roofit Toolkit for Data Modeling*, eConf C0303241 (2003) MOLT007, arXiv:physics/0306116

[142] K. S. Cranmer et al., *The Roostats Project*, PoS ACAT2010 (2010) 57.

[143] K. Cranmer, G. Lewis, L. Moneta, A. Shibata, and W. Verkerke, *Histfactory: A Tool for Creating Statistical Models for use with Roofit and Roostats*, CERNOPEN2012016 (2012)

[144] E. G. G. Cowan, K. Cranmer and O. Vitells, *Asymptotic formulae for likelihood-based tests of new physics*, `arXiv:1007.1727 [hep-ex]`.

[145] A. L. Read. *Presentation of search results: the CLs technique*. J. Phys. G: Nucl. Part. Phys., 28, 2002.

[146] A. L. Read. *Modified frequentist analysis of search results (the CLs method)*. In Proceedings of the First Workshop on Confidence Limits, CERN, Geneva, Switzerland, 2000.

[147] LHC Higgs Cross Section Working Group, S. Dittmaier, C. Mariotti, G. Passarino, R. Tanaka (Eds.), et al., *Handbook of LHC Higgs Cross Sections: 1. Inclusive Observables*, `arXiv:1101.0593 [hep-ph]`.

[148] LHC Higgs Cross Section Working Group, S. Dittmaier, C. Mariotti, G. Passarino, and R. Tanaka (Eds.), *Handbook of LHC Higgs Cross Sections: 2. Differential Distributions*, CERN-2012-002 (CERN, Geneva, 2012) , `arXiv:1201.3084 [hep-ph]`.

[149] ATLAS collaboration *Performance of the ATLAS Silicon Pattern Recognition Algorithm in Data and Simulation at $\sqrt{s} = 7$ TeV*, ATLAS-CONF-2010-072

[150] The ATLAS Collaboration, *A measurement of the material in the ATLAS inner detector using secondary hadronic interactions*, arXiv:1110.6191, JINST 7 (2012) P01013

[151] The ATLAS Collaboration, *Validation of the ATLAS jet energy scale uncertainties using tracks in proton-proton collision $\sqrt{s} = 7$ TeV*, ATLAS-CONF-2011-067

[152] The ATLAS Collaboration, *Track Reconstruction Efficiency in $\sqrt{s} = 7$ TeV Data for Tracks with $P_T > 100$ MeV* , ATL-PHYS-INT-2010-112

[153] D. de Florian, G. Ferrera, M. Grazzini and D. Tommasini, *Transverse-momentum resummation: Higgs boson production at the Tevatron and the LHC*, JHEP **1111** (2011) , `arXiv:1109.2109 [hep-ph]`.

[154] Statistical twiki, NuissanceCheck. https://twiki.cern.ch/twiki/bin/view/AtlasProtected/Nuisa